MODELING TURBULENCE IN LANDFILL GAS FLOW: INGRESS INTO A HORIZONTAL WELL

By

Abhishek Baral

A THESIS SUBMITTED IN PARTIAL FULFILMENT OF THE REQUIREMENTS FOR THE DEGREE OF

MASTER OF SCIENCE

IN

ENVIRONMENTAL SCIENCE

Thomson Rivers University

August 2021

Thesis Examining Committee:

Yana Nec

Thesis Supervisor

Department of Mathematics and Statistics

Thompson Rivers University

Rick Brewster

Department of Mathematics and Statistics

Thompson Rivers University

Mark Paetkau

Department of Physics

Thompson Rivers University

Tyler Huculak

GNH Consulting Ltd.

Abstract

Landfill gas collection is a salient component of waste management, energy recovery and environmental protection. The objective of the study is to improve the design and efficiency of operation of horizontal wells from the aspect of flow turbulence. Flow within the porous media (waste matrix, gravel) is coupled to the free pipe flow. Past studies performed this coupling without addressing the turbulence at the ingress to the well apertures. However, investigations at the apertures showed local fluctuations in pressure indicative of the importance of proper turbulence modeling. COMSOL Inc. Multi-physics simulation software is used to couple Darcy flow in the porous media with Reynolds averaged Navier-Stokes equations within the well using two turbulence models: $k - \varepsilon$ and $k - \omega$ closure models. The results were compared to semi-analytical solutions implemented in GNU Octave (Eaton *et al.*, 2020). The quasi-1D geometry employed in the semi-analytical model only accounted for the radial flow of gas and excluded the ingress turbulence effects. This study addresses such effects and the comparison plots from two solutions show the importance of including ingress turbulence.

A significant discrepancy in head losses within the well and across the landfill was observed between the two approaches. The cumulative ingress impact diminishes the suction strength required for adequate gas extraction as well as pinpoints the proximity of the intake apertures as the salient locus of head loss in the landfill mass. These effects are shown to impact the design and operational parameters of the horizontal well. Differences in the Reynolds number (found from the turbulence modeling results) showed the limitation of the quasi-1D geometry employed in the semi-analytical solutions. The velocity profiles at the ingress revealed abrupt changes indicative of adequate mesh refining and careful ingress flow modeling. Friction factor variation within the well showed the importance of careful ingress flow modeling. The study conclusively proved the importance of modeling turbulence and its underlying structures at the ingress for a realistic representation of flow in the horizontal wells.

Acknowledgements

I would first like to express my sincere gratitude to my supervisor Dr. Yana Nec for being incredibly patient with me over the years. Your support and guidance throughout this project helped me fulfill the work. Thank you for the regular meetings and your continuous drive to make me progress in the timely manner. Thank you for providing me with good exposure opportunities by guiding me though various conferences and seminars. I am extremely grateful for the graduate scholarship you allotted me from your research grants. It has been a true honor working as a student of yours.

I would also like to acknowledge the rest of my thesis supervising committee: Dr. Richard Brewster, Dr. Mark Paetkau and Tyler Huculak for their expertise and guidance. Thank you all for your amazing insights, ideas, comments and suggestions. I greatly appreciate Dr. Wendy Gardner, Dr. Lauchlan Fraser, Dr. Karl Larsen and Dr. Louis Gosselin for their guidance, lectures and support. Thank you so much for believing in me and providing me with all the support needed.

Finally, a very special thanks to all my friends and family for their continuous support. I am extremely grateful to my parents for their encouraging words, patience and support after all these years.

Contents

List of Figures

List of Tables

1. Introduction

Landfill gas (LFG) is a natural byproduct of an anaerobic decomposition within a landfill. LFG is comprised mostly of methane and carbon dioxide. It is regarded as a major contributor to climate change and also poses an environment and safety hazard because of its high flammability. This nature of the gas and its potential as an alternative energy necessitates an efficient gas collection system. LFG is collected through wells installed either vertically and/or horizontally in the landfill mass. The efficiency of a collection well is heavily contingent on the behavior of the gas as it flows through different system domains. Adequate understanding of this flow field will inform the optimization of different design and operational parameters of the well.

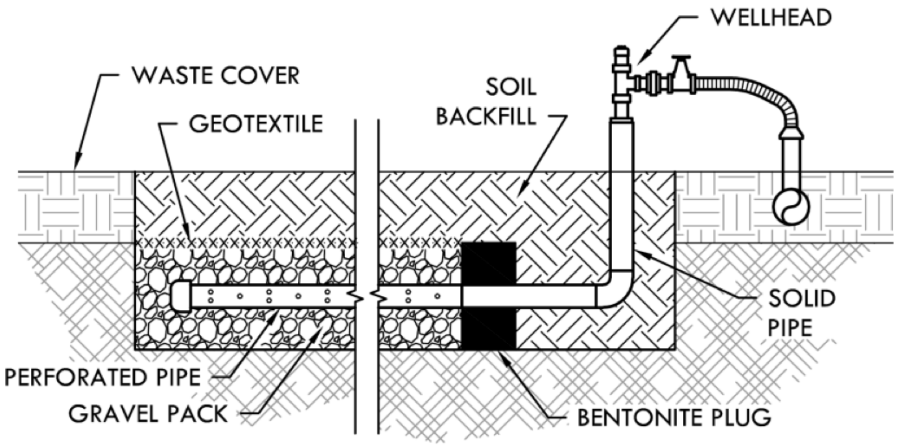

Figure 1.1: Horizontal gas well. (Figure 3-2 of EPA-US (2012))

Horizontal well consists of pipes that are laid horizontally in the landfill mass and are normally spaced 30 to 40m apart. These pipes are typically 10 to 20cm in diameter and are perforated in different sections along the length as shown in Figure 1.1. One end of the well is closed and at the other end vacuum is applied. The gas generated from the landfill mass is drawn into the well through the perforations as shown. Typically the well is enclosed with a layer of porous material such as gravel separating it from the

landfill itself. This layer is more permeable than the landfill mass and ensures flow of the gas into the well by preventing finer materials from the landfill mass obstructing the perforations in the well.

Physically, the system involves the flow through two porous media – gravel and waste – and through the pipe. The stream of gas entering the perforations undergoes directional changes and mixes with the crossflow within the well. This system is similar to the jet injection system where a homogeneous substance is injected into a crossflow. In that system the angle of entry and jet velocity are both controlled. The jet mixes with the crossflow via shearing between layers of fluid where the turbulent effects are dominant. In the horizontal well the stream of gas contracts as it passes through the narrow ingress apertures, then expands again while mixing with the crossflow. Unlike jet systems, the gas enters the well at a spectrum of angles and the velocity of the stream cannot be directly controlled at the ingress to the well. However 90° jet systems might be closely related to the flow at the ingress because majority of the stream enters the well at a 90° angle: the flow accelerates greatly toward the apertures, and the radial component of the velocity predominates at the entry. Even with numerous studies done on jet systems, qualitative understanding of jet injection cannot be reduced to simplistic analytical or empirical modeling. The behavior of flow at the ingress to the horizontal well cannot be any less complicated.

The construction and operation of this type of well has been historically done with very little mathematical insight. This has often resulted in an inefficient collection systems where sometimes the flow was uncontrollable or the collection was insufficient. The efficiency of a horizontal well in collecting the landfill gas depends strongly on understanding the behavior of gas as it enters the perforations. Nec & Huculak (2019) studied this system in a quasi-1D setting, excluding the effects of turbulence at the apertures. However the flow at the ingress is expected to be turbulent similar to the jet systems whose behavior and descriptions are explored in the next section. The purpose of this research was to gain qualitative insight into the impact of ingress turbulence on pressure distribution within the well and the surrounding flow domains. This will aid in the design and operation of an efficient horizontal well to continuously collect the landfill gas such that it does not escape into the atmosphere, thus impacting the amount of energy that can be recovered.

1.1 Literature Review

The understanding of turbulent behavior in flowing fluid is one of the most studied problems in classical physics. The chaotic changes in pressure and velocity are the defining features of turbulence. At the ingress the gas is drawn into the well through narrow ports of entry called holes or apertures. This flow system is similar in structure to the jet injection system and its mixing process, where a jet is injected into a crossflow. The regime of landfill gas flow is expected to be turbulent both within the well and at the ingress apertures, although for different reasons. This research focuses on the latter.

The problem of turbulence where a flow changes its direction has been studied by many researchers, suggesting approximate descriptions of turbulence for jet to crossflow injection systems. Direct Numerical Simulation (DNS) first coined by Smagorinsky (1963) involves numerically solving Navier-Stokes equations without any turbulence model and Large Eddy Simulation (LES) initially proposed by Orszag (1970) and first explored by Deardorff (1970) involves solving the same equations but filtering the smallest scales of turbulence. These methods are frequently used to study the jet injection systems. These computationally intensive works attempt to give a structure to an apparently chaotic nature of turbulence. Developments on jet trajectory equations, mixing, entrainment, effects of dimensionless parameters, optimal mixing parameters and flow field evolution are some of the topics. Although there are numerous studies done on jets, there is no agreement on an analytical model that describes this flow field. Since the gas entering into a horizontal well is similar to the jet injection, these studies could bear directly on modeling turbulence at the ingress of a horizontal well.

1.1.1 Turbulent Flow

One of the interpretations of turbulent flow is that it is possible to separate the random from non-random processes and that an organized motion could exist in an apparently chaotic flow (Roshko, 1976). Historical investigations into this flow have revealed interesting facts about it and the turbulent mixing process. The exploration of organized structures such as large eddies in a turbulent flow was provided primarily in Townsend (1956) and Grant (1958).

Turbulent mixing is a type of flow where two planar laminae of different fluid streams flow one above the other and are mixed by shearing. The hidden complex structures at the outer edges of large vortices are responsible for entrainment, a process where non-

turbulent fluid is incorporated into the turbulent region (Bevilaqua & Lykoudis, 1971). Nonetheless, the irrotational free stream has a role in exchanging momentum and energy: the irrotational fluid can leave the free stream as it is enfolded into and coalesces with the vortices. In the case of mixing of two gases of uniform densities, shadow pictures showed well-organized structures such as vortices in the cross-section (Roshko, 1976).

Presence of coherent structures in the turbulent boundary layer was discovered in the transition region by Emmons (1951). Turbulent jets might exhibit a mean flow having two rows of vortices of opposite signs. The vortex loop formed by joining of opposite vortex lines present in the turbulent boundary layer was dubbed 'horseshoe vortex' by Theodorsen (1952). This structure was more complex than the mean flow in the mixing layer where a row of vortices was of same sign. Thus, there was less possibility of forming three-dimensional structures in mixing layer unlike other shear flows. The development of small-scale three-dimensional structures and their relation to the two-dimensional vortices is described in the unpublished work referenced in Roshko (1976). At the time of the publication of Roshko (1976), it was impossible to simulate the two-dimensional mixing layer numerically for comparison with laboratory observations.

Townsend (1956) also inferred eddies of finite length elongated in the flow direction present in the turbulent boundary layer. These structures moved at a constant speed. The birth of vortices coincided with the demise of two or more older ones during a mixing process. These structures are also regarded as the basic elements of the turbulent boundary layer. The well organized, periodic component called vortex shedding was seen in the turbulent wake of a cylinder. This phenomenon persisted up to the highest Reynolds number (Re) measured. This number is defined as the ratio of inertial forces to viscous forces within the flowing fluid and can be written as:

$$\mathrm{Re} = \frac{\rho v l}{\mu}, \tag{1.1}$$

where ρ, v, l and μ are the density, flow speed, characteristic length and dynamic viscosity of the fluid. The vortices existed at much greater distances downstream, but with greater disorganization. Taneda (1959) observed the irregularity to appear in the wakes of vortex shedding in the transition range. This existed for a certain downstream distance. After that it reformed with the larger scale, suggesting an amalgamation process with the mixing layer. The change of scales occured only when a smaller vortex coalesced into a larger one, increasing the spacing to their immediate neighbors (Roshko, 1976). This interaction is the major contributor to the growth of the turbulent mixing layer.

In light of the above, the accurate description of the coherent structures, their role on the boundary layers and entrainment process might be crucial in estimating the effects of turbulence at the ingress of a horizontal well.

1.1.2 Structure and Flow Field

The flow within the horizontal well near the apertures is similar to jet mixing, where a jet is injected into a cross flow. There, the jet trajectories can be excellently predicted when the jet angle is either normal or less than 90° to the main channel, but as the injection angle progresses beyond 90°, the agreement between numerical results and the experimental data for jet trajectories deteriorates (Forney *et al.*, 1999).

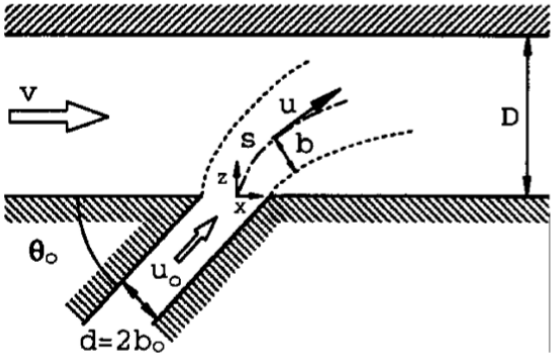

Figure 1.2: Two fluid streams mixing at an oblique branch. (Figure 1 of Forney *et al.*, 1999)

The configuration of a general pipeline mixer with an angle θ_0 is shown in Figure 1.2. There are four characteristic lengths that govern the trajectory of a jet within the tube: nozzle diameter d, tube diameter D, momentum length l_m and the near field length l_D. The momentum length l_m is given by the distance over which the jet travels before it bends over in the cross flow. It also stands for the distance within which the momentum flux of entrained fluid is comparable to its initial value at the orifice. The near field length l_D stands for the distance over which a parcel of fluid travels down the duct axis before it diffuses laterally over a distance comparable to the Prandtl eddy mixing length l. This length was described by Prandtl as the distance traversed by a fluid mass moving as a whole before it becomes completely blended in with the neighbouring masses of fluid. The correlation between the numerical and experimental results was excellent for cases with injection angles less than 90° downstream or perpendicular to the direction

of ambient mainstream flow. However the correlation deteriorates as the angle increases beyond 90° upstream.

At the apertures of a horizontal well, the landfill gas inflow is at a range of angles, since one aperture drains a large segment of the waste matrix. However, it stands to reason most fluid mass enters at 90°, given that the radial velocity component greatly dominates any longitudinal fluctuations. Thus, the correlation given in Forney *et al.*, 1999) might be useful in describing the trajectory of gas at the ingress.

A jet might take the form of two counter-rotating vortices aligned with the free stream (Kamotani & Greber, 1972). Then jet penetration, y, and vortex spacing, $2R$, varies as a power law of the downstream distance, x, with an exponent of about $\frac{1}{3}$. Integral methods were used to explain the jet's dynamics, but a difficulty was encountered in specifying the surface force including drag on control volume containing the jet. However, this difficulty could be overcome if the flow is treated as a pair of counter-rotating vortices. Durando (1971) developed a semi-empirical model for this region of flow.

Broadwell (1982) and Broadwell & Breidenthal (1982) proposed the models for turbulent mixing of the jets in stationary reservoirs and turbulent shear layers respectively, where mixing began with large scale intertwining of the two fluids. The initial mixing is followed by an inviscid cascade up to a Kolmogorov scale λ_0, after which the viscous effects become significant such that the dissipation of turbulent kinetic energy occurs via heat.

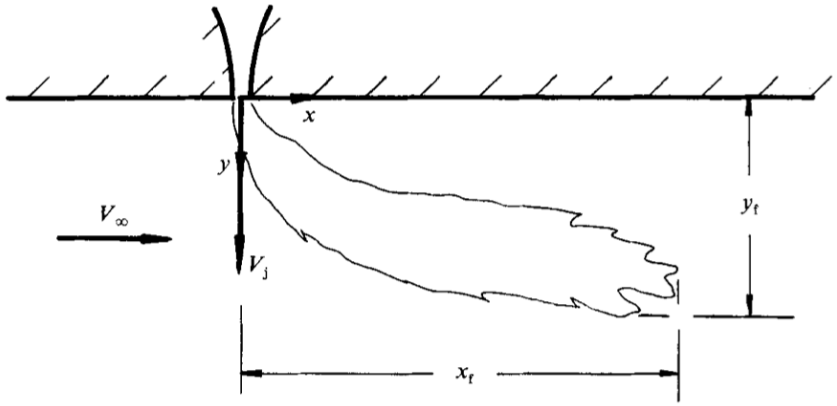

Figure 1.3: Flow geometry. (Figure 1 of Broadwell & Breidenthal, 1984)

Broadwell & Breidenthal (1984) gave a description of turbulent flow as a jet enters into the crossflow. The study explained the origin of the vortices and the flow in the far-field. A schematic diagram of a jet with density ρ_j and velocity V_j discharging normally

into the stream of density ρ_∞ and velocity V_∞ is shown in Figure 1.3. The lift force is indicated to generate a pair of counter-rotating vortices. In the experiment conducted, one-third power law was observed in flows at high Reynolds number. The flow was two-dimensional since the vortices move with the free stream and are approximately aligned with it in the farfield region. Then the relation among vertical velocity, impulse per unit length, the circulation of one vortex and the vortex-core separation are given.

As long as the plume of the jet is well discernible within the main stream it is referred to as a *flame*. The flame length was shown to be independent of the Reynolds number at higher values. For a low Reynolds number, the flame length was shown to be much longer because of sensitivity of the mixing rate to the presence of small scale turbulence. The mixing was said to be *strongly dependent* on the value of Re below a critical value. The alteration of the structure of the axisymmetric jet by the cross-flow generates vorticity, resulting in more efficient mixing. As the velocity of the stream increases from zero, it is linked with the formation of counter-rotating vortex pair or with a Taylor-Görtler instability. The resulting vortices were relatively large and consistent with the growth rate of a curved shear layer which implied rapid mixing and a short flame length.

Broadwell & Breidenthal (1984) finds that a nearfield description of the flow generated by a point force is lacking. They conclude that the measured flame length of the transverse jets is in agreement with the description of the farfield behavior. The power law, Reynolds number effects and turbulence scales described might be correlated to the turbulence at the ingress of a horizontal landfill gas well.

Stanley *et al.* (2002) studied a spatially evolving three-dimensional planar turbulent jets via direct numerical simulation. The governing equations for studying compressible, turbulent shear flows consisted of conservation equations for mass, momentum and energy. The hyperbolic tangent profile gave the longitudinal velocity in the shear layer on either side of the jet at the inflow. Energy to the flow field in a range of scales characteristic of that present in an actual turbulent flow was provided by inflow forcing. This forcing was done to increase the rate at which the jet develops from top-hat profile present at the inflow plane to the self-similar profiles downstream. The forcing was performed by generating a three-dimensional volume containing fluctuating solenoidal velocity, pressure and density fields. The simulation was performed using compressible Navier-Stokes equations. The mean and turbulence profiles near the outflow approached the expected self-similar values despite the relatively short stream wise domain length in the Direct Numerical Simulation (DNS).

Stanley *et al.* (2002) also discussed the small and large scale anisotropies in the jet. The small scale structures adjusted rapidly, whereas large scale structures adjusted slowly to the variations in local mean velocity gradients. The small scale structures were also more isotropic near the centerline of the jet. The mixing process was studied through probability density functions (PDFs) of the flow properties of a tracer. After the appearance of the vortical structures in the shear layers, the mixing process was dominated by large scale engulfing of fluid. The small scale mixing dominated further downstream in the turbulent core of the jet. An accurate computational model for a spatially evolving turbulent plane jet was developed using validated experimental data. This model was utilized in large eddy simulation (LES) by studying the two physical properties of turbulent planar jets: (a) the small scale anisotropy and (b) the evolution of the mixing properties of the jet. Along with the mean velocity and turbulence intensity profiles, development of shear layer structures into jet flow structures were documented by vorticity visualization and coherency spectra. The inflow condition had long-lived downstream effects on the development of turbulent flow fields.

In the experiments conducted, the Reynolds number based on jet width h at the nozzle increased from $\mathrm{Re}_h = 3000$ to $\mathrm{Re}_h = 4838$. The self-similar jet growth rate, $K_{1u} = 0.092$ and centerline velocity decay rate, C_{1u} agreed with the experimental data. The self-similarity in longitudinal velocity profiles and Reynolds stress profiles were seen at $x/h = 7.0$ and $x/h = 10.0$ respectively. The inflow fluctuation intensity and broadband spectrum provided rapid breakdown of the jet to the fully developed turbulent state. In the region $3.0 \leq x/h \leq 5.0$, there was a strong breakdown of three-dimensional structures in the jet. The balance of turbulent and kinetic energy in the self-similar region from the Direct Numerical Simulation also agreed well with the experimental data. The small scales of motion were substantially more isotropic in the centerline than at the jet edges. Near the nozzle, the PDF were dominated by small scale fluctuations. Further downstream and after rollup of strong vortical structures, the mixing process was dominated by the large scale engulfing of co-flow fluid into the jet. The influence of large scale engulfing of fluid on the mixing near the jet centerline progressively decreased downstream. In the core of the self-similar region, the small scale mixing dominated the mixing process. The work done by Stanley *et al.* (2002) shows that the DNS with high order space and time accuracy could be used to simulate the flow at the ingress to a horizontal well.

In a jet injection experiment, Patrick (1967) showed that the decay of jet source fluid

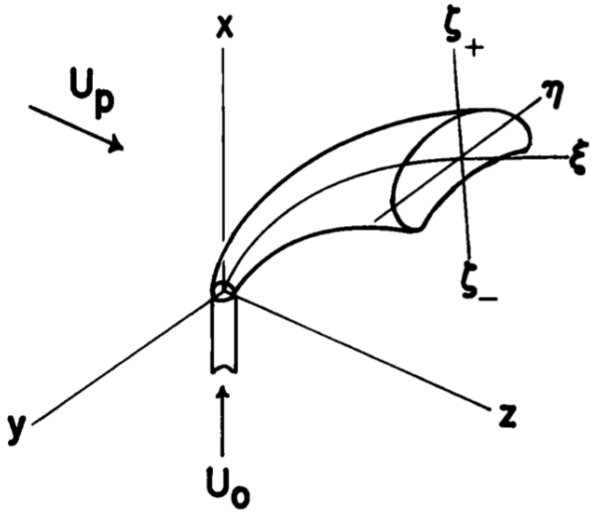

Figure 1.4: Coordinate systems for the jet flow. (Figure 1 of Rathgeber & Becker, 1983)

concentration along the jet trajectory depended on the ratio of the jet to mainstream initial speeds and is more rapid than on the centerline of a simple free jet. In an other experiment, a round subsonic jet was injected at a right angle through a port in the wall into a fully developed turbulent flow to obtain air-in-air mixing data (Rathgeber & Becker, 1983). Figure 1.4 shows the coordinate systems used to describe the jet flow. The position in the pipe was defined by Cartesian coordinates, x, y, and z with origin at the center of the jet entrance port, such that the x axis follows the jet injection tube centerline and z axis is parallel to the pipe centerline. Curvilinear coordinate system, ξ, η, ζ natural to the jet shape was used. The ξ axis appropriately represented the jet trajectory. Jet trajectories were measured, and the associated mixing field was characterized in terms of jet source fluid mean concentration and concentration fluctuations. Concentration fluctuation spectral density, integral scale, and intermittency were studied. The mean velocity field of the jet was obtained experimentally and theoretical models for the jet trajectory were developed. Jet trajectories, spreading rates, and dilution rates were correlated empirically with dimensionless input parameters.

Jet entrance core was found to be typically wasted within two to three entry port diameters and the initially circular jet cross section was distorted to a kidney shape due to counter-rotating vortices. The jet then rapidly attained a direction and mean speed close to that of transverse stream, and the counter-rotating vortices expanded over the whole jet cross-section. The stream longitudinally bifurcated and exhibited lateral max-

ima of the source fluid concentration on either side of the plane of symmetry. Once fully deflected, it evolved into a flow structure dominated by the parallel vortex pair moving with the mainstream velocity. Due to the proximity of the pipe wall, however, such a regular vortex structure was limited. The mainstream turbulence was presumed to promote jet dispersion and wall boundary layer to allow greater jet penetration. The mixing field was explored in cylindrical polar coordinates. These results accurately represented the gas/gas mixing process.

The jet trajectory was reasonably well correlated with downstream position in the pipe (Rathgeber & Becker, 1983). Observed trajectories showed more rapid jet deflection since the jet mixing was influenced by the crossflow turbulence. Increased deflection in the jet was attributed to the adverse pressure gradients which inhibited jet penetration. Larger jets were also subjected to stronger crossflow effects over their initial development length of $2-3$ source diameters and this partly explained slightly lower jet penetrations at higher pipe Reynolds number. Large concentration eddies of the jet in a cross-flow were elongated along the radial direction. Such eddies were stretched longitudinally in a free jet with stagnant surroundings. Bifurcation of the jet was also represented. Each plume formed a distinct continuous convoluted boundary that separated it from the other; the intermittency observed on the ξ axis was rather due to the presence of large eddies or islands of pipe stream fluid entrained into the central region of the jet.

Mass-average velocity of the fluid in a pipe flow, mass flux of that fluid, pipe flow Reynolds number and relative pipe roughness were sufficient to define the equilibrium pipe flow velocity distribution (Rathgeber & Becker, 1983). Effects of pipe flow Reynolds number and pipe relative roughness were expected to be minor at high Reynolds number. Pipe diameter was the most useful scale after the jet reached opposite wall of the pipe. Then, the wall influence became appreciable. Thus, different effects on the flow could be expected due to varying Reynolds number along the length of a horizontal gas well.

1.1.3 Mixing

Mixing transition which is regarded as a universal phenomenon of turbulence in turbulent jet mixing (Dimotakis, 2000), can also be expected at the ingress of the horizontal well. The resulting turbulent flow requires a minimum value of the Reynolds number to be sustained. As the Reynolds number is increased to that value, a growing interfacial area between the mixing species is generated. This is called the *mixing transition*. This transition occurs in shear layers and is also found in jets.. Mixing transition is distinct

from laminar to unsteady flow transition. The latter reflects the inability of the flow to remain stable with increasing Reynolds number whereas the former occurs beyond those Reynolds number and is characterized by subsequent, well defined, further transition in the flow. There are three stages of turbulent mixing: the entrainment stage, the stirring stage and the molecular mixing stage. For high Schmidt number flows, distinguishing between vorticity-diffusion stage and species-diffusion stage is useful.

In shear layer flows, Konrad (1977) noted that the transition to three-dimensional structures occur at a particular value of the Reynolds number associated with the ability of a flow to sustain a three-dimensional fluctuation. The appearance of streamwise longitudinal lines and a 'dimpling' of the surface occured at a Reynolds number of approximately 10^4 (Dimotakis, 2000, Figure 1). This transition was abrupt with an increase in disorganized three-dimensional structures. Stronger mixing was observed for higher Reynolds number. Streamwise vortices and three-dimensionality of the flow indicated a well mixed state, which was nominally two-dimensional in the inflow region. The velocity fluctuations followed a power law regime in the energy spectrum. An additional distance downstream was anticipated for the mixing, which indicated even higher local Reynolds number.

In case of the jets, well mixed states were less clearly visible than in the shear layers. Separation of shear layers was documented only as a near-field behavior of the jets. Even at low Reynolds numbers, this flow was three-dimensional. A qualitative transition in the turbulent-mixing behavior for Re near 10^4 was found. In the case of a liquid jet, the flow transitioned to a better mixed state as the Reynolds number increased beyond $\mathrm{Re}_{\mathrm{min}} \approx 10^4$. Hence, $\mathrm{Re}_{\mathrm{min}} = 10^4$ was a necessary but not sufficient condition for the flow to be in a fully developed state. However, this dependence was weaker in the case of a gas jet. This difference in the behavior was attributed to the Schmidt number effect. Transitional Reynolds number for the jets was twice as large for the shear layers. However, it became comparable when the characteristic length scale $\delta(x)$ was chosen as a local radius. Since the Reynolds number for turbulent jets is given by the product of two stochastic variables: local velocity and length scale, the value is ill defined.

Dahm & Dimotakis (1987) investigated the entrainment and mixing in the self-similar far field of a steady, axisymmetric, momentum driven, turbulent jet in water. Laser Induced Fluorescence (LIF) techniques were used. In the case of shear layers, the mixing resulting from dynamics of nearly periodic large scale vortical motions was observed. This large scale organization transported the unmixed fluid from both free streams across the

entire extent of the layer.

In the case of turbulent jets, the flame length fluctuations and the concentration profiles revealed unmixed ambient fluid throughout the jet. This indicated a large scale organization in the jet far-field. The organization was capable of bringing unmixed ambient fluid deep into the jet. The probability of detecting it at a point on the jet increased approximately at regular intervals which was consistent with periodic large scale entrainment. At high Schmidt number, this probability, however decreased with increasing Reynolds number. For the gas jets with Sc $\cong$ 1, diffusion layer thickness was approximately equal to Kolmogorov scale. At such small scales of flow, less unmixed ambient fluid was expected. Thus, the flow to the ingress of a horizontal well is likely to follow large scale organization depending on Reynolds number and Schmidt number effects as discussed.

For the mixing with a crossflow setting, a jet injected at 90° angle was as good as any other injection systems investigated (Chilton & Genereaux, 1930). Fitzgerald & Holley (1979) studied several such systems and their mixing characteristics. Effect of secondary currents on a system, their power requirements and optimum conditions were discussed. Two types of system originating at the pipe wall were studied: (1) single jet with injection angles ranging from 90° to 150° and (2) double jets with injection angle at 90° placed diametrically opposite on the pipe wall.

A turbulent jet injection with significant momentum across the ambient flow reduces the mixing distance by creating rapid initial mixing. For single jet systems with injection angles greater than 90°, the jets are turned upstream against the ambient flow causing vigorous shearing. This caused the optimum 150° jet to undergo more initial mixing than the optimum 90° jet. Increasing the angle from 90° to 150°, decreased the mixing distance by 35% but at the cost of large increase in the momentum ratio and in the power requirement.

For the optimum mixing in dual jets system, momentum ratio for each jet was on the order of one-half of the optimum momentum ratio for a single jet injection. Although, it did not produce a significant decrease in the mixing distance, this system required less power than a single jet.

Swirling motion by a fixed propeller was also induced in the upstream to study the effects of secondary currents on different systems. For a single 90° jet, swirl deflected the jet toward the side of the pipe which caused an asymmetrical distribution in concentration. This asymmetry increased the mixing distance despite an increase in radial

diffusion coefficient. Unlike the single jet injection, swirl decreased the mixing distance for the dual jets. The swirl caused a greater amount of initial mixing because the jets got deflected in the opposite directions and did not merge at the center which explained the shorter mixing distance.

Based on the findings, using three or more jets in a system was expected to provide a factor of safety against possible effects of secondary currents. Even though, single jet provided enough mixing for sufficient pipe lengths, the speed was comparatively slower (Fitzgerald & Holley, 1979). The flow of landfill gas into the horizontal well might be relatable to the turbulent mixing behavior observed for jet injection systems as discussed.

1.1.4 Stream Junction

The flow at the ingress of the landfill wells is similar to a T junction of the pipe flow system as shown in the Figure 1.5. The junction includes the branch and main passage pipe sections as shown. Unlike this system, the flow at the ingress is not confined by the perpendicular branch section and the gas enters the well at a spectrum of angles. However the majority of the stream can be assumed to enter the well at 90° angle because of the high flow speeds near the ingress. Thus a 90° pipe juncture model was used to explain the fluid behaviour at the ingress.

This pipe junction is characterized by the turbulent mixing of the streams, accompanied by the pressure losses (Idelcik, 1966). In the course of this mixing, the exchange of momentum takes place between the particles moving at different velocities resulting in the equalization of the velocity distributions in the common stream. Exchange of kinetic energy occurs between the streams flowing in the junction. The loss of total pressure during this process is always large and positive if the fluid in the branch has high velocity. This results in the positive resistance coefficient defined as the ratio of the difference of total pressures to the mean dynamic pressures in the given section. In this junction, losses due to curving of the stream are added to the losses due to mixing. These losses are mainly due to stream separation from the inner wall, which leads to contraction of incoming streams at the point of turn and its subsequent expansion. Two kinds of losses can be noted:

a) the loss due to mixing.

b) the loss due to 90° turn.

The resistance coefficient of the branch through which the lower-velocity stream moves can have a negative value. The resistance coefficient in the junction can then be calculated

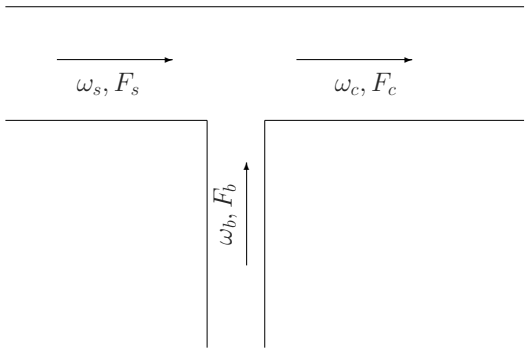

Figure 1.5: Tee junction of a pipe (recreated from Idelcik (1966, p. 266))

by the following formula, given by Levin (1935, 1940) and refined by Taliev (1952):

$$\zeta_b = \Delta H_b \frac{2g}{\gamma {\omega_b}^2} = \frac{\zeta_{c.b}}{\left(\frac{Q_b}{Q_c}\frac{F_c}{F_b}\right)^2}, \tag{1.2a}$$

where ζ, ΔH, g, γ, ω Q and F are the resistance coefficient, pressure loss, acceleration due to gravity, specific gravity of the fluid, mean velocity, discharge and cross-sectional area. The variables $\zeta_{c.s}$ and $\zeta_{c.b}$ are the resistant coefficients of the main passage and branch expressed in terms of velocity in the common channel. The suffixes s, b and c correspond to the main passage, branch and common channel respectively. In the branch, the coefficient is given by:

$$\zeta_{c.b} = \Delta H \frac{2g}{\gamma {\omega_c}^2} = A\left[1 + \left(\frac{Q_b}{Q_c}\frac{F_c}{F_b}\right)^2 - 2\left(1 - \frac{Q_b}{Q_c}\right)\right] = A\zeta'_{c.b}, \tag{1.2b}$$

where $\zeta'_{c.b}$ is determined from the curves $\zeta'_{c.s} = f\left(\frac{Q_b}{Q_c}\right)$ at different $\frac{F_b}{F_c}$ and A is taken from the table at different $\frac{F_b}{F_c}$(Idelcik, 1966, p. 266).

Similarly, the coefficient in the main passage is given by:

$$\zeta_{c.s} = \Delta H_s \frac{2g}{\gamma {\omega_c}^2} \cong 1.55 \frac{Q_b}{Q_c} - \left(\frac{Q_b}{Q_c}\right)^2, \tag{1.2c}$$

which is determined by the curve given as (Idelcik, 1966, p. 266):

$$\zeta_{c.s} = f\left(\frac{Q_b}{Q_c}\right), \tag{1.2d}$$

which holds for all practical values of F_b/F_c and

$$\zeta_s = \Delta H_s \frac{2g}{\gamma {\omega_s}^2} = \frac{\zeta_{c.s}}{\left(1 - \frac{Q_b}{Q_c}\right)^2}. \tag{1.2e}$$

It can be noted that the cross sectional area of the branch section is much lower compared to main passage in the horizontal landfill gas well. An attempt was made to make quantitative modifications to Eqs. (1.2a) – (1.2e) in order to reconcile the semi-analytical solution of Nec & Huculak (2019) with the finite element solutions obtained in the current research project. The discrepancies in the two results are discussed further in the later sections.

2. Methods

Based on the literature discussed, it is expected that landfill gas entry into the collection well is turbulent due to an abrupt change of direction and mixing with the crossflow within the well and between faster and slower layers outside the ingress aperture. This causes local fluctuations in pressure along the well, directly impacting the extraction of the gas. Turbulence modeling can provide an accurate picture of the behavior of the gas inside the well and thus allow for maximization of collection efficiency. Techniques like DNS and LES provide an accurate description of turbulence at those sections but come at a cost of being highly computationally intensive. In this study, less computationally intensive models ($\kappa-\epsilon$ and $\kappa-\omega$) for Reynolds averaged Navier-Stokes (RANS) equations are solved using a finite element solver (COMSOL Inc., 2018). The purpose is to gain qualitative insight into turbulence at the ingress and its overall impact on the pressure distribution within the well and the surrounding coupled porous media. The solutions obtained are compared with the quasi-1D semi-analytical solution (Nec & Huculak, 2019) that does not address ingress turbulence effects.

2.1 Horizontal Landfill Well

The horizontal gas well collection system is comprised of three flow domains (waste, gravel and the pipe). The gas generated from the waste flows through the porous matrices - waste and gravel - and into the pipe where the flow is unobstructed. The pipe segments before and after each slits were closed to the immediate porous medium boundary. In those segments, turbulence due to wall friction is the primary cause of the decrease in the vacuum potential (head) along the length of the well which is termed as the *head loss*. Turbulence at the ingress due to mixing and bending of incoming fluid stream is the secondary cause of head loss. The flow geometry in Figure 2.1 shows the perforated pipe imbedded within media of distinct permeability. Set the origin $(r, \ell) = (0, 0)$ at the center of the pipe within the outlet plane. The perforated sections are located at points ℓ_i, $i = \{1, \ldots, N\}$, numbered from the outlet.

At the outlet of the well, sub-atmospheric pressure p_o is imposed and the other end is kept blocked. The imposed suction draws in the gas through the apertures as shown.

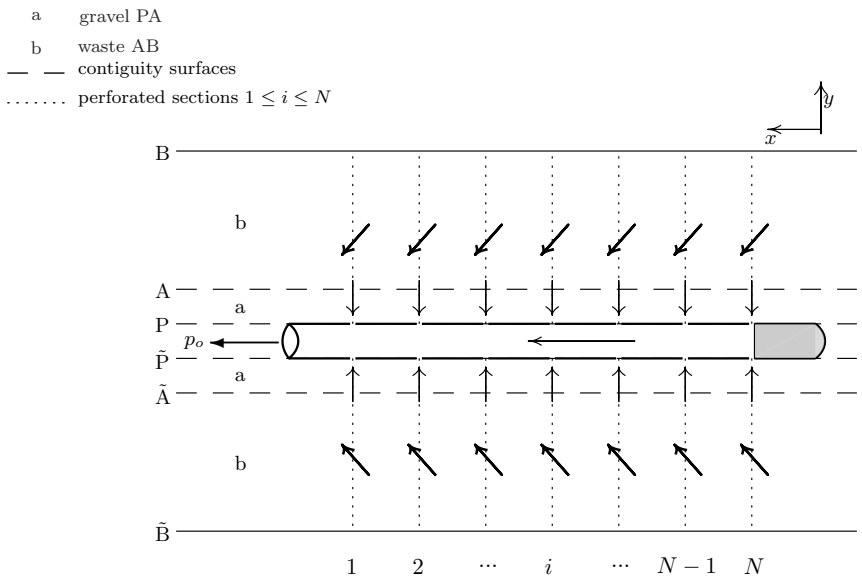

Figure 2.1: Side view of the flow geometry (Figure 1(a) of Nec & Huculak (2019))

The flow within the porous media strongly depends on the permeability of the matrix and can be very complex for a realistic representation of the flow. Although reality does not support the assumption that the matrix is isotropic, it is reasonable to take an *effective* value for its permeability. The main physical argument in favour thereof is that it is simply impossible to provide a more accurate description, since the content of the waste and the degree of its local compaction cannot be controlled in any way, not at the inception of any one landfill and definitely not during its lifetime. Apertures of realistic shape, i.e. holes, are converted to slits in both the semi-analytical and COMSOL models, in order to maintain the axial symmetry of the geometry.

2.1.1 Semi-Analytical Model

In the semi-analytical model (Nec & Huculak, 2019), the landfill utilising a horizontal well was comprised of a perforated pipe at the center surrounded by gravel (Figure 2.1). The gas generating waste extended radially from this core.

The quasi-one dimensional solution were based on a purely radial flow within each plane perpendicular to a perforated cross section. The porous medium flow was coupled

to unobstructed pipe flow. The pipe segments are numbered respectively (Figure 2.1), so that segment i is delimited by $[\ell_{i-1},\ \ell_i]$ with $\ell_0 = 0$ corresponding to the outlet, and carrying mass $\dot{m}_i$. Conservation of mass must hold at each perforated section ℓ_i. Suppose $\Delta\dot{m}_i$ denotes the mass incoming at section i. Then

$$\dot{m}_{i-1} = \dot{m}_i + \Delta\dot{m}_{i-1}, \quad i = \{2,\ ...,\ N\}. \tag{2.1a}$$

Continuity of pressure implies

$$p\left(r_p^+, \ell_i\right) = p\left(r_p^-, \ell_i\right), \quad i = \{1,\ ...,\ N\}, \tag{2.1b}$$

where $p\left(r_p^+, \ell_i\right)$ is the pressure at aperture in position ℓ_i as given by the porous medium flow and $p\left(r_p^-, \ell_i\right)$ is the pressure at the same point as given by the unobstructed pipe flow.

These apertures were represented as axisymmetric slits of an area equivalent to that of a prescribed number of circular holes. The resulting slit width was sufficiently narrow to reduce the entire landfill to a sequence of thin generating discs aligned with the slits. Whilst it is useful in obtaining a reasonable estimate of the well functionality owing to its quick convergence and easy implementation in the freely available software (Eaton *et al.*, 2020), it fails to provide finer optimization of the turbulent flow regime at the ingress, because the flow field transversal to the solid pipe boundary away from the perforated sections is inaccessible.

2.1.2 COMSOL Model

COMSOL Inc. (2018) is a simulation software that uses a finite element solver to solve coupled systems of partial differential equations in conventional physics based interfaces. It provides an integrated development environment and unified workflow for fluid mechanics applications with the ability to couple multiple physics environments. It requires building a model, assigning proper physics module and boundary conditions. In order to reduce the required computing resources for realistic models, appropriate actions such as axisymmetric geometry, section-wise geometry, mesh refining etc are considered during model building. For this model, the geometry of the well was constructed in axisymmetric (two-dimensional) cylindrical coordinates.

The horizontal well system was fully sealed at the outermost waste boundary. The

flow regime was constrained within the two porous media and the pipe domains. The flow of the gas into the well was only allowed through distinct narrow slits whilst keeping the rest of the pipe boundary blocked. Zero flux boundary conditions were imposed in those remaining sections and also at the blocked and outlet planes (bar the pipe outlet itself). This formulation differed from the quasi-1D geometry employed in the semi-analytical model where the entire landfill mass was a sequence of generating discs aligned with the slits. This discrete representation of landfill mass in semi-analytical model created an equivalence to a flow of gas through the entire contiguity surface such that the blocked sections were absent. The resultant impact due to the difference in geometries employed in two models is discussed in detail in the following chapter.

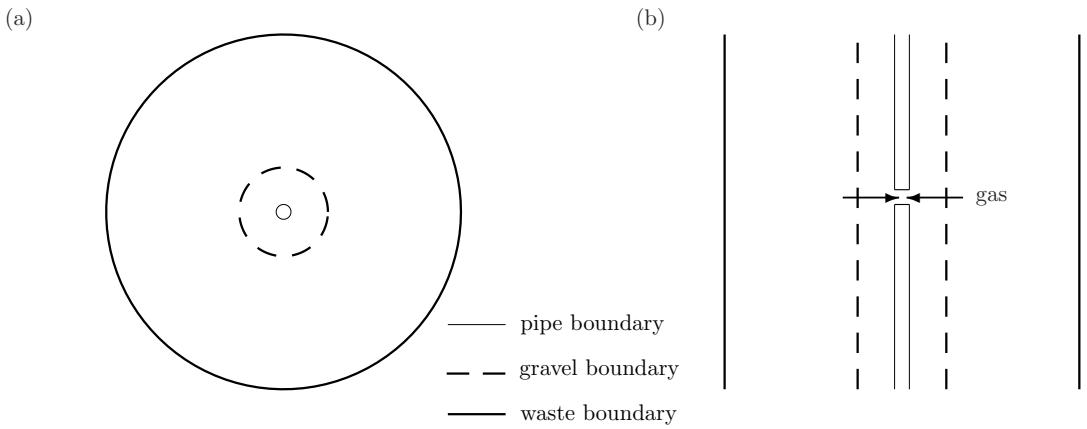

Figure 2.2: Horizontal well schematic: cross-section (a) and longitudinal view (b).

The schematic of the horizontal well used in COMSOL is shown in Figure 2.2. The full model geometry was constructed as follows. A single longitudinal section of Schedule 40 pipe is used as a unit block to form the full well. The dimensions for this pipe are given in Table 2.1. The pipe is closed at one end and the outlet pressure, p_o is applied at the open end. In a real well the perforations are circular holes in the pipe wall. To retain axial symmetry in the geometry, gravity was not incorporated as a bulk force and the perforations were simplified by using slits of equivalent size.

Figure 2.3(a) shows the apertures in a single cross section of the pipe and Figure 2.3(b) shows the slit of equivalent surface area. The first and last slits were at 15m from both ends of the pipe. All other slits were spaced 15m apart. These slits had the radial dimension equal to the pipe wall thickness t and the longitudinal dimension w. The value w is determined by equating the area of perforations in a section to the area of the slit required:

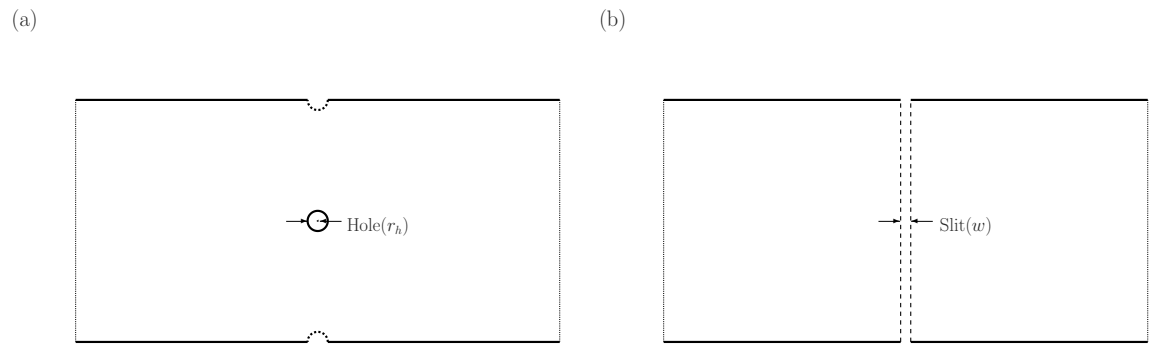

Figure 2.3: Holes (a) and its equivalent slits (b) in the well section.

$$n_h \pi {r_h}^2 = 2\pi r_p w$$
$$\therefore \quad w = n_h \frac{{r_h}^2}{2r_p}, \tag{2.2}$$

where n_h is the number of holes per section, r_h is the hole radius and r_p is the radius of the pipe. In COMSOL, Darcy's flow module was assigned for the porous media and two turbulence models ($k-\epsilon$ and $k-\omega$) were used to model the pipe flow which included the ingress effects. The governing equations and the analytical descriptions are discussed in the following sections.

All the parameters used to describe the fluid and the flow domains are listed in Table 2.1. To address the compressibility effects of the gas, ideal gas law was incorporated within COMSOL such that it computed the density of the gas which is based on the value of pressure at each node along the entire length of the well. To couple the Darcy's law within the porous media and the turbulent flow within the well, a single pressure variable was assigned at the contiguity region of the ingress and the gravel. This was then verified using the principle of mass conservation for the whole system, i.e. the generated mass of gas was equalled to the mass at the outlet.

Parameter	Symbol	Value	Test range
Dynamic viscosity	μ	1.4×10^{-5}Pa·s	
Specific gas constant	R	287J/(kg·K)	
Pipe radius	r_p	0.0762m (3in)	
Gravel domain radius	r_g	1m	
Waste domain radius	r_w	10m	
Pipe wall thickness	t	0.007112m (0.28in)	
Total length of the well	L	420m	
Hole radius	r_h	0.00635m (0.25in)	
No. of holes per section	n_h	6	$2n_h$
No. of slits in L	N	27	$2N + 1$
Temperature	T	15°C	
Outlet pressure (open end)	p_o	100800Pa	$(p_o - 200, p_o + 300)$
Generation rate	Q	1.1×10^{-6}kg/(m^3·s)	
Porosity	ϕ	0.55	
Permeability of gravel layer	k_1	3.2×10^{-5}m^2	
Permeability of waste layer	k_2	1.5×10^{-8}m^2	

Table 2.1: Parameters used to create the full model.

2.1.3 Laminar Pipe flow

Laminar flow is characterized by fluid layers moving smoothly past the adjacent layers such that mixing among the layers is absent. These flows are devoid of complex mixing structures and are much easier to describe mathematically. The laminar flow through a pipe of circular cross-section is known as the Hagen-Poiseuille flow. The equations for this type of flow can be derived from the Navier-Stokes momentum equations in 3D cylindrical coordinates (r, θ, x). Navier-Stokes equation in vector form are written as:

$$\frac{D(\rho\vec{u})}{Dt} = -\vec{\nabla}p + \rho\vec{g} + \mu\nabla^2\vec{u}, \tag{2.3}$$

where $\frac{D(\rho\vec{u})}{Dt} = \left(\frac{\partial(\rho\vec{u})}{\partial t} + \nabla\cdot\left(\rho\vec{u}\vec{u}^{\mathrm{T}}\right)\right)$ is the material derivative of $\rho\vec{u}$. ρ is the fluid density, $\vec{u}$ is the velocity vector, $\vec{\nabla}p$ is the pressure gradient, ∇^2 is the Laplace operator and $\vec{g}$ represents body accelerations acting on the fluid continuum such as gravity. The continuity equation in (r,θ,x) is:

$$\frac{1}{r}\frac{\partial}{\partial r}(ru_r) + \frac{1}{r}\frac{\partial(u_\theta)}{\partial\theta} + \frac{\partial(u_x)}{\partial x} = 0, \tag{2.4}$$

where u_r, u_θ and u_x are the cylindrical velocity components in r,θ and x directions respectively. For a steady, axisymmetric, fully developed flow with gravity neglected, Eqs. (2.3) and (2.4) reduce to:

$$\frac{1}{r}\frac{\partial}{\partial r}\left(r\frac{\partial u_x}{\partial r}\right) = \frac{1}{\mu}\frac{\mathrm{d}p}{\mathrm{d}x}. \tag{2.5a}$$

For simplicity, the pressure gradient, $\frac{\mathrm{d}p}{\mathrm{d}x} = \frac{p_\ell - p_o}{\ell} = \nabla_x p$, where p_ℓ and p_o are the pressures at inlet and outlet of the pipe. Integrating Eq. (2.5a) on both sides gives:

$$r\frac{\partial u_x}{\partial r} = \frac{r^2}{2\mu}\nabla_x p + c_1, \tag{2.5b}$$

where c_1 is the first integration constant. At $r = 0$ the derivative $\frac{\partial u_x}{\partial r} = 0$ because the velocity must be a smooth function. Thus $c_1 = 0$. Eq. (2.5b) becomes:

$$\frac{\partial u_x}{\partial r} = \frac{r}{2\mu}\nabla_x p. \tag{2.5c}$$

Integrating Eq. (2.5c), gives:

$$u_x = \frac{r^2}{4\mu}\nabla_x p + c_2, \tag{2.5d}$$

where c_2 is the second integration constant. At $r = R$, $u_x = 0$, thus $c_2 = -\frac{R^2}{4\mu}\nabla_x p$. Eq. (2.5d) reduces to:

$$u_x = \frac{1}{4\mu}\nabla_x p(r^2 - R^2). \tag{2.6}$$

Parameter	Symbol	Value
Pipe radius	R	0.02m
Pipe length	ℓ	0.3m
Inlet pressure	p_l	0.02Pa
Outlet pressure	p_o	0Pa
Dynamic viscosity	μ	1.82×10^{-5}Pa· s
Density	ρ	1.2kg/m^3

Table 2.2: Parameters used to create the first model. cf. Table 2.1

As a verification step, a simple laminar pipe flow was modeled to obtain the velocity profiles of the flow at different sections of a cylindrical pipe. The velocity profiles obtained from Eq. (2.6) and COMSOL are compared and discussed in the next chapter. Table 2.2 shows all the parameters used to obtain the solutions for this model.

2.1.4 Porous Media Flow

The basic law that governs the flow through a porous medium is called Darcy's law. This law relates velocity and pressure gradient and thus acts as the momentum equation in the porous medium flow, the same role Navier-Stokes equations play in the continuum flow. For the landfill gas, it is possible to use the ideal gas equation:

$$p = \rho R T, \tag{2.7}$$

where p, ρ, R and T denote the fluid pressure, density, specific gas constant and temperature, respectively. The flow of gas in the two porous media – the waste layer and gravel layer – obeys Darcy's law, which in the absence of gravity can be written as:

$$\vec{u} = -\frac{k}{\mu}\nabla p, \tag{2.8}$$

where $\vec{u}, \mu$ and ∇p denote the velocity vector, dynamic viscosity and pressure gradient for the gas flowing over a given radial distance in the medium of permeability, k. The permeability takes different effective values for each layer. The conservation of mass equation can be written as:

$$\nabla \cdot (\rho \vec{u}) = Q, \tag{2.9}$$

where Q denotes the mass generation rate. Combining Eqs. (2.7),(2.8) and (2.9) gives:

$$\frac{1}{r}\frac{\mathrm{d}}{\mathrm{d}r}\left(r\left(\frac{-k}{\mu}\right)\frac{\mathrm{d}p}{\mathrm{d}r}\frac{p}{RT}\right)=Q. \tag{2.10a}$$

Since k and μ are constant within each domain, Eq. (2.10a) can be rewritten as:

$$\frac{\mathrm{d}}{\mathrm{d}r}\left(r\frac{\mathrm{d}p}{\mathrm{d}r}p\right)=-\frac{\mu}{k}RTQr. \tag{2.10b}$$

Integrating Eq. (2.10b),

$$p\frac{\mathrm{d}p}{\mathrm{d}r}=-\frac{\mu}{k}RTQ\frac{r}{2}+\frac{\tilde{a}}{r}. \tag{2.10c}$$

Integrating Eq. (2.10c),

$$p^2=a\ln r+b-\frac{\mu}{k}RTQ\frac{r^2}{2}, \tag{2.11}$$

where a and b are the integration constants. This analytical solution was successfully reproduced in COMSOL for a set of parameters listed in Table 2.3.

Parameter	Symbol	Value	Test range
Pipe radius	r_p	0.0762m	
Gravel radius	r_g	0m, 1m	
Waste radius	r_w	3m, 10m	
Gas constant	R	287J/(kg·K)	
Dynamic viscosity	μ	1.4×10^{-5}Pa·s	
Temperature	T	15°C	
Pressure at innermost gravel	p_g	100818Pa	
Pressure at outermost waste	p_w	101325Pa	
Generation rate	Q	0kg/(m^3·s)	(0,Q+20)
Permeability of gravel layer	k_1	3.2×10^{-5}m^2	
Permeability of waste layer	k_2	3.2×10^{-6}m^2	

Table 2.3: Parameters used to create the second and third models. cf. Table 2.1.

2.1.5 Turbulence in Pipes

In fluid dynamics, the Darcy-Weisbach equation relates the pressure loss due to friction along the given length of pipe to the average velocity of the fluid flow for an incompressible fluid. In other words, this equation addresses the turbulence impact on the pressure due to the friction of the pipe wall for an incompressible fluid. In a cylindrical pipe of uniform diameter d, flowing full, the pressure loss due to viscous effects Δp is proportional to length ℓ, and the Darcy-Weisbach equation in pressure loss form can be written as:

$$\Delta p = \frac{1}{2}\rho u^2 f \frac{\ell}{d}, \tag{2.12}$$

where ρ, u and f are the density of the fluid, flow velocity and the Darcy friction factor. The Darcy friction factor, f can be obtained from various equations depending on the flow regime in the domain. The well known Colebrook equation expresses the Darcy friction coefficient f as a function of Reynolds number Re and non-dimensional roughness of the pipe inner surface, ϵ both based on the pipe diameter (Colebrook, 1939):

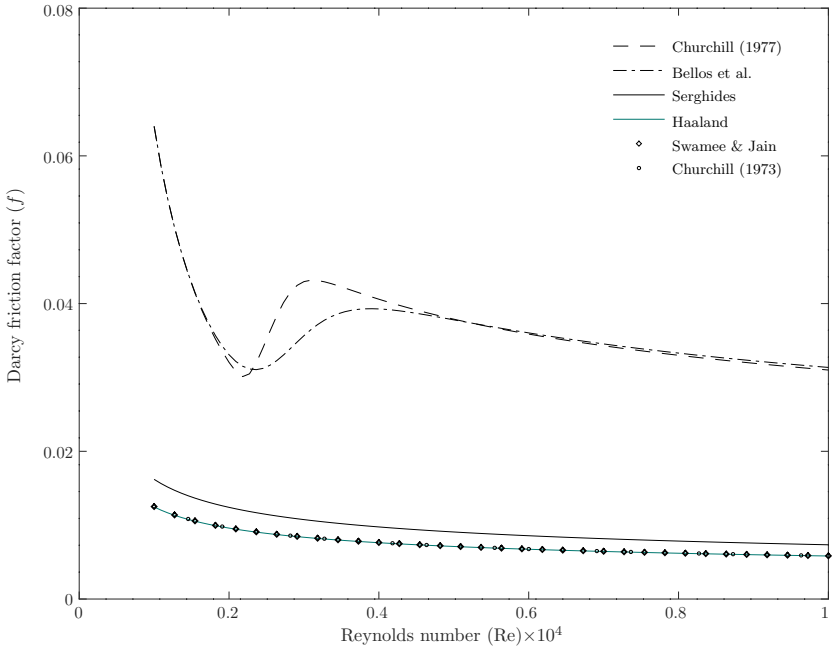

Figure 2.4: Friction factor versus Reynolds number by different empirical approximations.

$$\frac{1}{\sqrt{f}} = -2\log\left(\frac{\epsilon}{3.7} + \frac{2.51}{\mathrm{Re}\sqrt{f}}\right). \tag{2.13}$$

The solution of this equation is implicit, which is usually done numerically. There are various approximations of the implicit Colebrook equation. Some of the variations are:

1. Swanee & Jain (1976)

$$f = \frac{0.25}{\left[\log\left(\frac{\epsilon}{3.7} + \frac{5.74}{\mathrm{Re}^{0.9}}\right)\right]^2}; \tag{2.14a}$$

2. Churchill (1973)

$$\frac{1}{\sqrt{f}} = -2\log\left(\frac{\epsilon}{3.715} + \left(\frac{6.943}{\mathrm{Re}}\right)^{0.9}\right); \tag{2.14b}$$

3. Churchill (1977)

$$\frac{f}{8} = \left[\left(\frac{8}{\mathrm{Re}}\right)^{12} + \frac{1}{(\Theta_1 + \Theta_2)^{1.5}}\right]^{\frac{1}{12}}, \tag{2.14c}$$

where

$$\Theta_1 = \left[-2.457\ln\left(\left(\frac{7}{\mathrm{Re}}\right)^{0.9} + 0.27\epsilon\right)\right]^{16} \quad \text{and} \quad \Theta_2 = \left(\frac{37530}{\mathrm{Re}}\right)^{16};$$

4. Haaland (1983)

$$\frac{1}{\sqrt{f}} = -1.8\log\left[\left(\frac{\epsilon}{3.7}\right)^{1.11} + \frac{6.9}{\mathrm{Re}}\right]; \tag{2.14d}$$

5. Serghides (1984)

$$\frac{1}{\sqrt{f}} = \Psi_1 - \frac{(\Psi_2 - \Psi_1)^2}{\Psi_3 - 2\Psi_2 + \Psi_1}, \tag{2.14e}$$

where

$$\Psi_1 = -2\log\left(\frac{\epsilon}{3.7} + \frac{12}{\mathrm{Re}}\right),\ \Psi_2 = -2\log\left(\frac{\epsilon}{3.7} + \frac{2.51\Psi_1}{\mathrm{Re}}\right) \quad \text{and}$$

$$\Psi_3 = -2\log\left(\frac{\epsilon}{3.7} + \frac{2.51\Psi_2}{\mathrm{Re}}\right);$$

6. Bellos *et al.* (2018)

$$f = \left(\frac{64}{\mathrm{Re}}\right)^a \left[0.75\ln\frac{\mathrm{Re}}{5.37}\right]^{2(a-1)b} \left[0.88\ln 3.41\frac{1}{\epsilon}\right]^{2(a-1)(1-b)}, \tag{2.14f}$$

where

$$a = \frac{1}{1+\left(\frac{\mathrm{Re}}{2712}\right)^{8.4}} \quad \text{and} \quad b = \frac{1}{1+\left(\frac{\mathrm{Re}}{150}\epsilon\right)^{1.8}}.$$

Comparison plot for friction factors computed for Re in the range of $1000 - 10000$ from Eqs. (2.14a) – (2.14f) is shown in Fig. 2.4. From all the plots, Serghides (1984) is known to provide the best estimate for the friction factor in the turbulent regime.

Two turbulence models are used for simulating single-phase flows within the well. The equations solved are the Reynolds-averaged Navier-Stokes (RANS) equations for conservation of momentum and the continuity equation for conservation of mass. The RANS equations are time-averaged equations of motion for fluid flow. They are derived from the instantaneous Navier-Stokes equations by using Reynolds decomposition, i.e. separation of the flow variable such as velocity into the mean (time averaged) component and the fluctuating component. The continuity equation and the Navier-Stokes Eq. (2.3) after neglecting the body acceleration $\vec{g}$ can be written as:

$$\nabla\cdot(\rho\vec{u}) = 0 \tag{2.15a}$$

and

$$\frac{\partial(\rho\vec{u})}{\partial t} + \nabla\cdot\left(\rho\vec{u}\vec{u}^{\mathrm{T}}\right) = -\nabla p + \mu\nabla^2\vec{u}. \tag{2.15b}$$

Flow variables $\vec{u}$ and p from Eq. (2.15b) can be split into the sum of mean ($\langle\rho\vec{u}\rangle, \langle p\rangle$) and fluctuating ($(\rho\vec{u})', p'$) parts:

$$\rho\vec{u} = \langle\rho\vec{u}\rangle + (\rho\vec{u})' \quad \text{and} \quad p = \langle p\rangle + p'. \tag{2.16a}$$

According to the Reynolds rules, the mean of the fluctuating quantity is zero:

$$\langle(\rho\vec{u})'\rangle = \langle p'\rangle = 0. \tag{2.16b}$$

Averaging the Eq. (2.15a) gives:

$$\langle\nabla\cdot(\rho\vec{u})\rangle = \nabla\cdot\langle\rho\vec{u}\rangle = 0 \tag{2.16c}$$

and

$$\nabla\cdot(\rho\vec{u}) = \nabla\cdot(\langle\rho\vec{u}\rangle + (\rho\vec{u})') = \nabla\cdot(\rho\vec{u})' = 0. \tag{2.16d}$$

Similarly averaging the Eq. (2.15b) gives:

$$\frac{\partial\langle\rho\vec{u}\rangle}{\partial t} + \langle\nabla\cdot\left(\rho\vec{u}\vec{u}^{\mathrm{T}}\right)\rangle = -\nabla\langle p\rangle + \mu\nabla^2\langle\vec{u}\rangle. \tag{2.16e}$$

Here,

$$\langle\nabla\cdot\left(\rho\vec{u}\vec{u}^{\mathrm{T}}\right)\rangle = \langle\rho\vec{u}\rangle\cdot\nabla\langle\vec{u}\rangle^{\mathrm{T}} + \langle(\rho\vec{u})'\cdot\nabla\vec{u}'^{\mathrm{T}}\rangle. \tag{2.16f}$$

Since $\nabla\cdot(\rho\vec{u}'\vec{u}'^{\mathrm{T}}) = (\rho\vec{u})'\cdot\nabla\vec{u}'^{\mathrm{T}} + \vec{u}'^{\mathrm{T}}\nabla\cdot(\rho\vec{u})' = (\rho\vec{u})'\cdot\nabla\vec{u}'^{\mathrm{T}}$, the RANS equation independent of coordinate system from Eq. (2.16e) becomes:

$$\frac{\partial\langle\rho\vec{u}\rangle}{\partial t} + \langle\rho\vec{u}\rangle\cdot\nabla\langle\vec{u}\rangle^{\mathrm{T}} = -\nabla\langle p\rangle + \mu\nabla^2\langle\vec{u}\rangle + \nabla\cdot\langle-\rho\vec{u}'\vec{u}'^{\mathrm{T}}\rangle, \tag{2.17}$$

where $\langle-\rho\vec{u}'\vec{u}'^{\mathrm{T}}\rangle \equiv \sigma_R$ is the Reynolds stress tensor. The time evolution equation of Reynolds stress is very complex. Finding out the value of the Reynolds stress has been a subject of intense modeling and interest for most of the past century. The problem is recognized as a closure problem. While there have been numerous attempts to develop good models for Reynolds stress, when solving the fluid equations using computational

fluid dynamics, often the simplest turbulence models have proved the most effective. Such models include $k-\epsilon$ and $k-\omega$ turbulence models.

The $k-\varepsilon$ Model

The $k-\varepsilon$ model is one of the most used turbulence models for industrial applications. The COMSOL turbulent $k-\varepsilon$ module uses the standard $k-\varepsilon$ model given in Wilcox *et al.* (1998). This model includes two additional transport equations and two dependent variables: the turbulent kinetic energy k and its dissipation rate ε. The turbulent viscosity, μ_T is modeled as:

$$\mu_T = \rho C_\mu \frac{k^2}{\varepsilon}, \tag{2.18a}$$

where C_μ is a model constant. The transport equation for k is given as:

$$\rho\frac{\partial k}{\partial t} + \rho\vec{u}\cdot\nabla k = \nabla\cdot\left(\left(\mu + \frac{\mu_T}{\sigma_k}\right)\nabla k\right) + P_k - \rho\varepsilon, \tag{2.18b}$$

where the production term is

$$P_k = \mu_T\left(\nabla\vec{u} : \left(\nabla\vec{u} + (\nabla\vec{u})^{\mathrm{T}}\right) - \frac{2}{3}(\nabla\cdot\vec{u})^2\right) - \frac{2}{3}\rho k\nabla\cdot\vec{u}. \tag{2.18c}$$

The transport equation for ε is given as:

$$\rho\frac{\partial \varepsilon}{\partial t} + \rho\vec{u}\cdot\nabla\varepsilon = \nabla\cdot\left(\left(\mu + \frac{\mu_T}{\sigma_\varepsilon}\right)\nabla\varepsilon\right) + C_{\varepsilon 1}\frac{\varepsilon}{k}P_k - C_{\varepsilon 2}\frac{\rho\varepsilon^2}{k}. \tag{2.18d}$$

The model constants in Eqs. (2.18a), (2.18b) and (2.18d) are determined from experimental data (Wilcox *et al.*, 1998) and the values are listed in Table 2.4. Eqs. (2.18b) and (2.18d) are implemented by including an upper limit on the mixing length, $l_{\mathrm{mix}}^{\mathrm{lim}}$:

$$l_{\mathrm{mix}} = \max\left(C_\mu\frac{k^{3/2}}{\varepsilon}, l_{\mathrm{mix}}^{\mathrm{lim}}\right). \tag{2.18e}$$

The mixing length is used to calculate the turbulent viscosity. The $k-\varepsilon$ turbulence model relies on several assumptions. These assumptions limits the accuracy of the model but it

Constant	Value
C_μ	0.09
$C_{\varepsilon 1}$	1.44
$C_{\varepsilon 2}$	1.92
σ_k	1.0
σ_ε	1.3

Table 2.4: $k-\epsilon$ model constants

is considered a fair tradeoff for the amount of computational resources saved compared to other complicated turbulence models.

The $k-\omega$ Model

The $k-\omega$ model in COMSOL solves for the turbulent kinetic energy k and for the dissipation per unit turbulent kinetic energy ω commonly known as the specific dissipation rate. The CFD Module in COMSOL has the Wilcox *et al.* (1998) revised $k-\omega$ model which can be written as:

$$\rho\frac{\partial k}{\partial t}+\rho\vec{u}\cdot\nabla k=P_k-\rho\beta^*k\omega+\nabla\cdot((\mu+\sigma^*\mu_T)\nabla k), \tag{2.19a}$$

$$\rho\frac{\partial \omega}{\partial t}+\rho\vec{u}\cdot\nabla \omega=\alpha\frac{\omega}{k}P_k-\rho\beta\omega^2+\nabla\cdot((\mu+\sigma\mu_T)\nabla \omega), \tag{2.19b}$$

where the turbulent viscosity (μ_T) is given by:

$$\mu_T=\rho\frac{k}{\omega},$$

and the closure coefficients are given as:

$$\alpha = \frac{13}{25}, \quad \beta = \beta_0 f_\beta, \quad \beta^* = \beta_0^* f_{\beta^*}, \quad \sigma = \frac{1}{2}, \quad \sigma^* = \frac{1}{2},$$
$$\beta_0 = \frac{13}{125}, \quad f_\beta = \frac{1+70\chi_\omega}{1+80\chi_\omega}, \quad \chi_\omega = \left|\frac{\Omega_{ij}\Omega_{jk}S_{ki}}{(\beta_0^*\omega)^3}\right|,$$
$$\beta_0^* = \frac{9}{100}, \quad f_{\beta^*} = \begin{cases} 1 & \chi_k \leq 0 \\ \dfrac{1+680\chi_k^2}{1+400\chi_k^2} & \chi_k > 0 \end{cases}, \quad \chi_k = \frac{1}{\omega^3}(\nabla k \cdot \nabla \omega), \tag{2.19c}$$

where Ω_{ij} is the mean rotation-rate tensor:

$$\Omega_{ij} = \frac{1}{2}\left(\frac{\partial \vec{u_i}}{\partial x_j} - \frac{\partial \vec{u_j}}{\partial x_i}\right), \tag{2.19d}$$

and S_{ij} is the mean strain-rate tensor

$$S_{ij} = \frac{1}{2}\left(\frac{\partial \vec{u_i}}{\partial x_j} + \frac{\partial \vec{u_j}}{\partial x_i}\right). \tag{2.19e}$$

P_k is given by Eq. (2.18*c*). The following auxiliary relations for the dissipation ε and the turbulent mixing length l_* are also used:

$$\varepsilon = \beta^* \omega k \quad l_{\text{mix}} = \frac{\sqrt{k}}{\omega}. \tag{2.19f}$$

2.2 Mass Conservation

The coupling of the two physics systems in different flow domains was done by using continuity of pressure at the contiguity surface separating the well and the immediate gravel medium. The imposed pressure continuity at the surface allowed the suction at the outlet to maintain distinct pressure gradient at all slits, which in turn was the pressure condition for Darcy's law for the rest of the porous media. This also implied that the velocity parameter was continuous at the boundary, although this was not specified during the model building.

The coupling was verified by confirming the mass conservation for the whole system. In other words, mass generated from the landfill must be equal to the mass at the outlet.

The mass flow rate, $\dot{m}$ at the outlet can be obtained as:

$$\dot{m} = \int_{\text{area}} \rho v \, \mathrm{d}A = \frac{p_o}{RT} \int_0^{2\pi} \int_0^{r_p} vr \, \mathrm{d}r\mathrm{d}\theta = 2\pi \frac{p_o}{RT} \int_0^{r_p} vr \, \mathrm{d}r, \tag{2.20}$$

where p_o, v and r_p are the outlet pressure, the longitudinal velocity at the outlet and the radius of the pipe respectively. The differential area $\mathrm{d}A = r \, \mathrm{d}r\mathrm{d}\theta$. The mass flux within the waste domain can be obtained from:

$$\dot{M} = VQ = \pi(r_w^2 - r_g^2)\ell Q, \tag{2.21}$$

where $V = \pi(r_w^2 - r_g^2)\ell$ is the volume of the waste domain and Q is the mass generation rate for the waste domain. The verification is discussed in the following chapter.

3. Results and Discussion

3.1 Preliminary Results

3.1.1 Laminar Flow

As a preliminary verification problem for pipe flow, Hagen-Poiseuille flow was modeled to obtain the radial velocity profiles for different sections along the length of the pipe. The results obtained using COMSOL model and Eq. (2.6), the analytical solution for laminar flow are compared in Fig. 3.1.

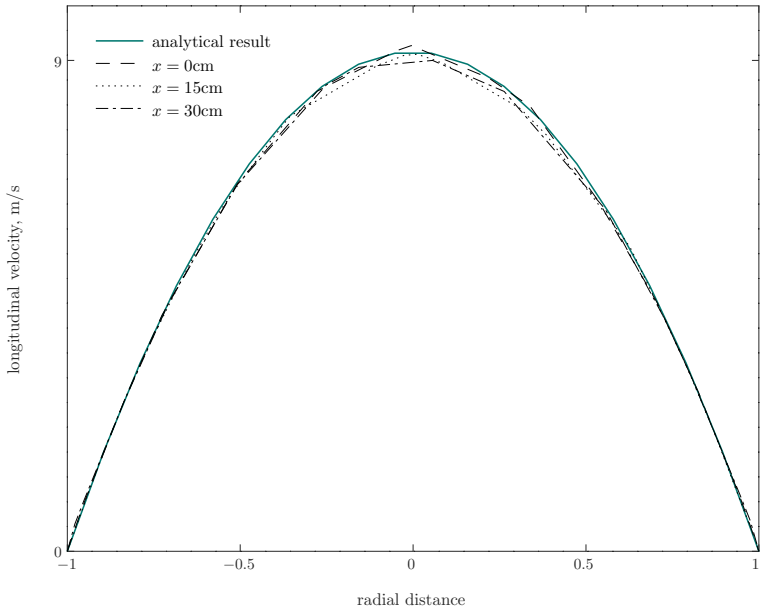

Figure 3.1: Comparison of velocity profiles at different sections on the horizontal pipe.

COMSOL profiles were obtained by solving Navier-Stokes equations for conservation of momentum and continuity equation for conservation of mass. All the parameters used to construct the model in COMSOL are listed in Table 2.2. The agreement between the two solutions show that the COMSOL is a reliable solver to study pipe flows.

3.1.2 Porous Media Flow

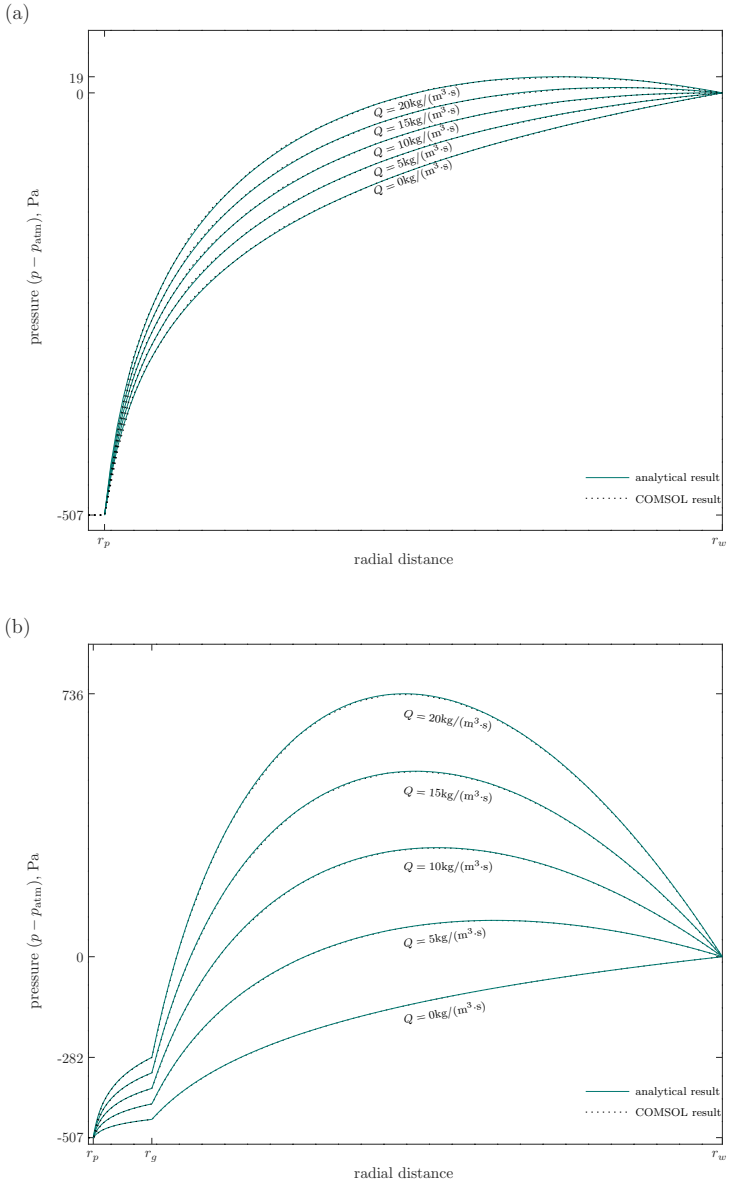

Figure 3.2: Radial change of pressure in the waste ($r_w = 3\text{m}$) (a) and in the gravel and waste ($r_w = 10\text{m}$) (b). The values r_p, r_g and r_w are the radii of the pipe, gravel and waste respectively. All parameters used are listed in Table 2.3.

As a preliminary verification problem for porous media flow, two models consisting of a pipe surrounded by one and two concentric porous media were created in the COMSOL. In both systems, sub-atmospheric pressure was applied at the innermost boundary and

atmospheric pressure was maintained at the extreme porous medium boundary. For a flow through a single layer of waste, the variations in pressure as calculated using Eq. (2.11) are compared with COMSOL results as shown in the Figure 3.2(a).

Similarly Eq. (2.11) is also used to obtain the change of pressure in two porous media (waste and gravel). This is compared with the COMSOL results and given in Figure 3.2(b). Both figures show that the analytical solutions agree well with the COMSOL results. The mass generation rate Q within the waste domain was increased monotonically for both systems. Restricting the increased rate of flow by keeping the domain's permeability constant resulted in a subsequent pressure build up as shown. The radial distance at which the pressure attains a maximum is regarded as the radius of influence for the collection well, beyond which the applied suction for the generating mass no longer collects gas.

3.2 Combined Turbulent Model

The full COMSOL model consisting of three concentric domains with slits as described in the previous chapter was built. Parameters listed in Table 2.1 were used to construct the well, its surrounding porous media and assign boundary conditions. Two turbulence models, $(k-\varepsilon)$ and $(k-\omega)$, were used for simulating single-phase flows at high Reynolds numbers (COMSOL Inc., 2018) using Reynolds-averaged Navier-Stokes (RANS) equations and solving for conservation of mass and momentum. The turbulence effects are modeled by closing the RANS equations using the aforementioned models. Within the porous media, the flow was modeled using Darcy's law. Coupling between the porous media and pipe flow domains was done at the contiguity surfaces between fluid in the pipe and gravel layer (slits) by using a single pressure variable for both physics systems. The slit has a radial dimension of t, the thickness of the pipe, and a longitudinal dimension of w, the width of the slit, obtained from Eq. (2.2).

The size and the number of the slits were both increased to analyze its effects on the flow field. A range of parameters such as outlet suction, permeabilities of the porous matrix and mass generation rates were also scanned, seeking similarities and qualitative differences in flow behaviour. The obtained results are then compared with the semi-analytical model given by Nec & Huculak (2019).

3.2.1 Longitudinal Variation

Pressure and Density

To analyze the variation of pressure within the well, a range of vacuum was assigned at the outlet of the COMSOL model. These conditions maintained the sub-atmospheric

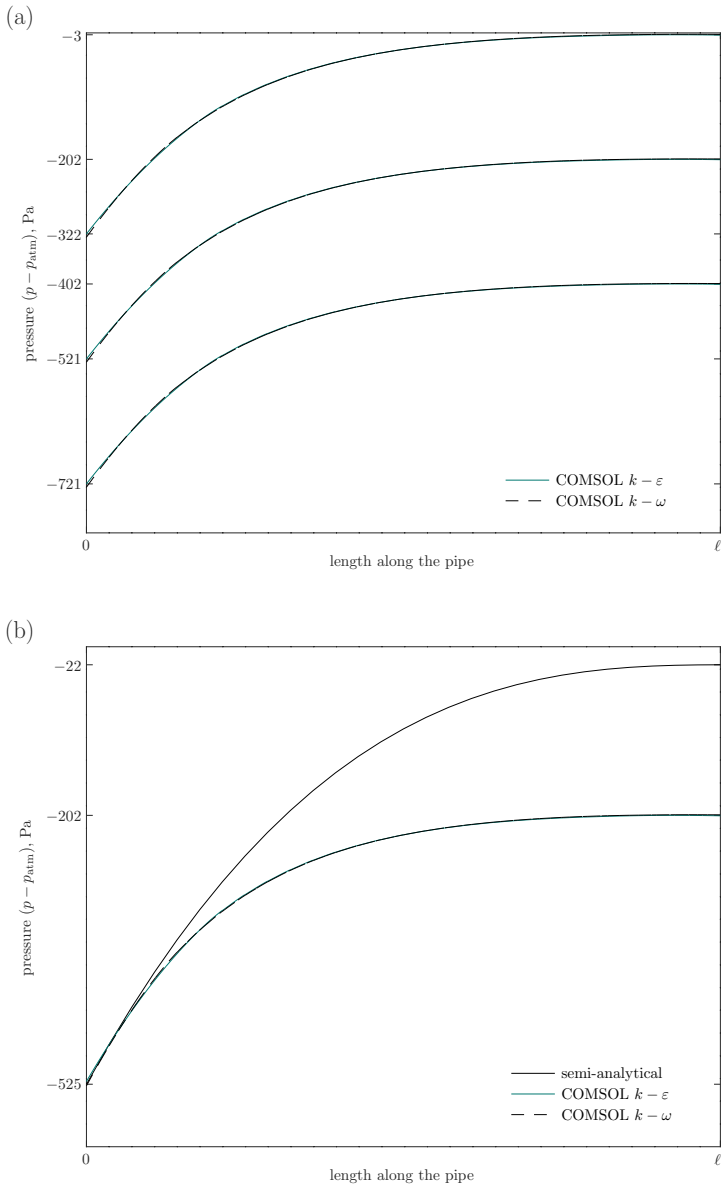

Figure 3.3: Longitudinal pressure variation at p_o = 100.6kPa, 100.8kPa and 101kPa monotonically from bottom to top for two different turbulence models in COMSOL (a) and comparison with the semi-analytical solution at the outlet pressure of 100.8kPa along the length of the pipe (b). The values x = 0m and $x = l$ = 420m corresponds to the outlet and the blocked end of the pipe respectively.

pressure throughout the coupled system of the porous media and the well. Figure 3.3(a) shows the longitudinal pressure profiles along the centerline of the well at different vacuum conditions. Clearly the profiles are qualitatively similar. This similarity holds valid for different sets of permeabilities and mass generation rate parameters. No visible differences can be seen in the results obtained using the two turbulence models.

Figure. 3.3 (b) shows the longitudinal pressure profiles along the centerline of the well for the two turbulence models and quasi-1D semi-analytical model. The overestimation of the head loss by the latter model is indicative of excluding turbulent effects at the apertures.

To analyze how pressure varied within the landfill at a fixed radial distance from the well, semi-analytical and turbulent solutions were compared and shown in Figure 3.4. For this purpose, only the $k - \varepsilon$ solution is shown, since both models give visually indistinguishable results. Figure 3.4 (a) exhibits two *plateaux*, i.e. the longitudinal pressure gradient is zero at both ends of the landfill. The semi-analytical solution cannot reproduce this feature at the outlet plane because the quasi-1D geometry cannot accommodate a no flux condition on the outlet plane outside the pipe. In the COMSOL solution the continuity of pressure is imposed only at the slits, such that the blocked sections of the pipe at both ends of the well cause the pressure gradient to be zero. The variation predicted by the turbulent model is small and sub-atmospheric, as is seen from juxtaposing the two in the same panel as shown in Figure 3.4(b). The comparison of the two solutions in 3.4 (b) clearly illustrates the semi-analytical model's prediction of high pressure field within the landfill domain at the same outlet vacuum. This overestimation within the landfill mass can be attributed to the limitation of the quasi-1D geometry employed in the semi-analytical model. This formulation was devoid of any narrow geometries (slits) and the continuity of flow was imposed by excluding the ingress effects entirely, such that the *head loss* was predicted to occur radially within the porous media. This resulted in qualitative extension of longitudinal pressure changes within the well (Figure 3.3(b)) to the porous media surrounding it (Figure 3.4(b)). Investigations done using COMSOL revealed that the inclusion of slits as a contiguous flow domain is essential and its vicinity accounts for the significant amount of changes in the flow field. These changes near the slits are illustrated and discussed in the later sections.

Because the density of the gas is a function of the pressure, the profiles for the longitudinal variation of density within the well are qualitatively similar to Figure 3.3(b) and are not shown.

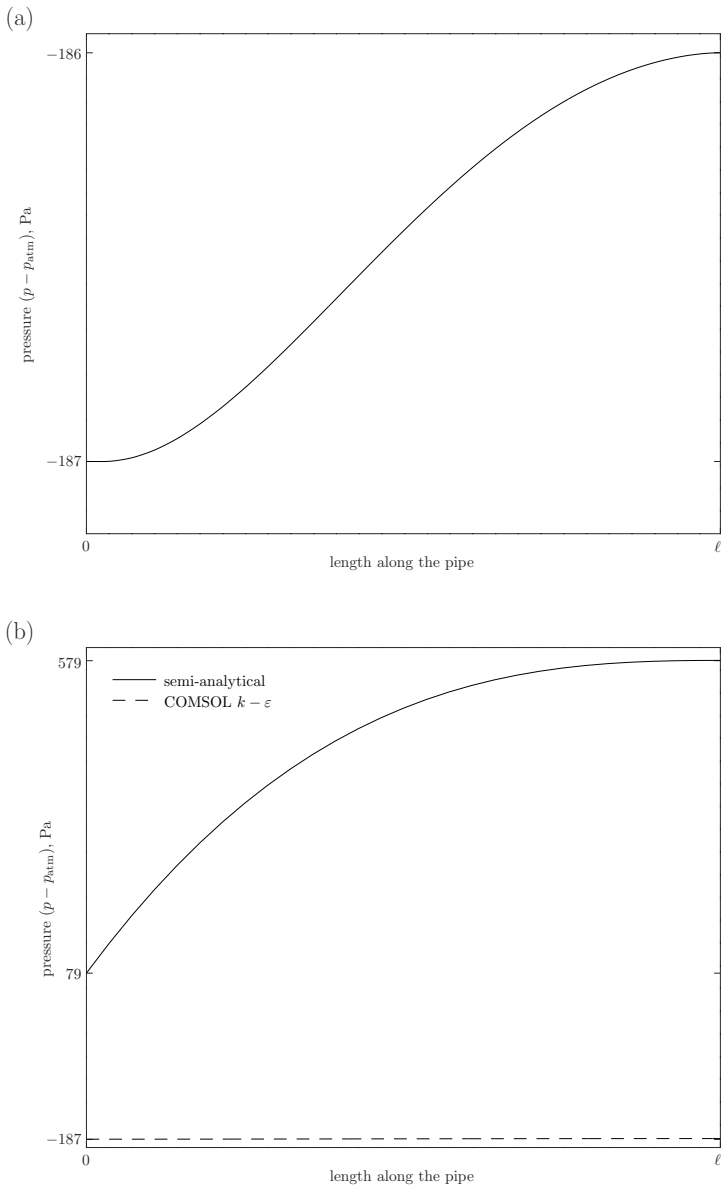

Figure 3.4: Pressure variation along the length of the pipe at 5m radial distance and at $p_o = 100.8$kPa obtained using COMSOL (a), and its semi-analytical counterpart (b). The values $x = 0$m and $x = l = 420$m corresponds to the outlet and the blocked end of the pipe respectively.

Therefore, the inclusion of ingress turbulence is essential in providing an accurate description of the flow field. The COMSOL pressure profiles show that the sub-atmospheric pressure is maintained in/around the well with very small vacuum or less power as compared to the predictions from semi-analytical model.

Reynolds Number and Velocity

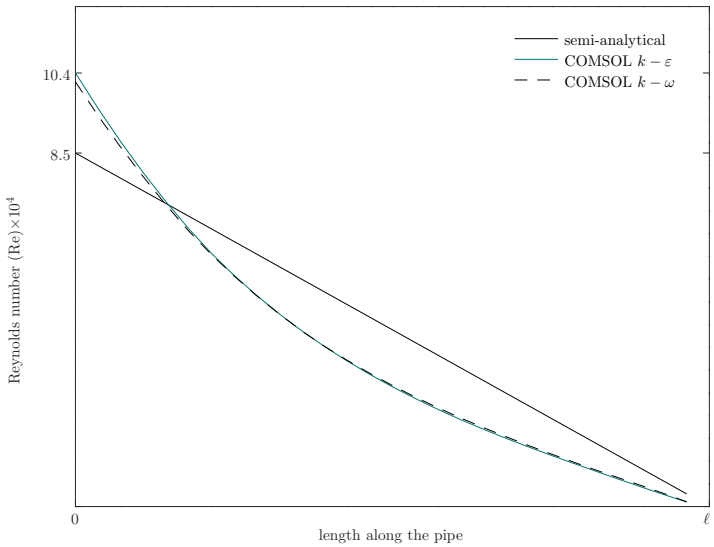

Figure 3.5: Longitudinal variation of Reynolds number for two different turbulence models in COMSOL compared with the semi-analytical solution at $p_o = 100.8$kPa. The values $x = 0$m and $x = l = 420$m corresponds to the outlet and the blocked end of the pipe respectively.

The Reynolds number was calculated using Eq. (1.1). Here the characteristic length is taken as the diameter of the pipe d and the density was obtained from $\rho = p/RT$. Figure 3.5 shows the longitudinal variation of Reynolds number within the well along its centerline using COMSOL and semi-analytical models. The turbulent models predict the non-linear variation of the Reynolds number. In the semi-analytical model, the mass entering the well at each aperture is almost equal and the contiguity surface was throughout the whole pipe boundary. This corresponds to the ostensibly linear profile as shown. The COMSOL model, however, predicts a fully non-linear variation. The non-linearity at the middle section of the well is characteristic of the mass flowing through only the specific parts of the pipe boundary (slits), whilst the rest of the pipe boundary was blocked. COMSOL models also predict a much higher value of Reynolds number at the outlet. The Reynolds number profiles from the COMSOL solutions, exclude local fluctuations at the slit sections. The averaged profile was obtained using the custom written Octave function (A.1).

Friction Factor

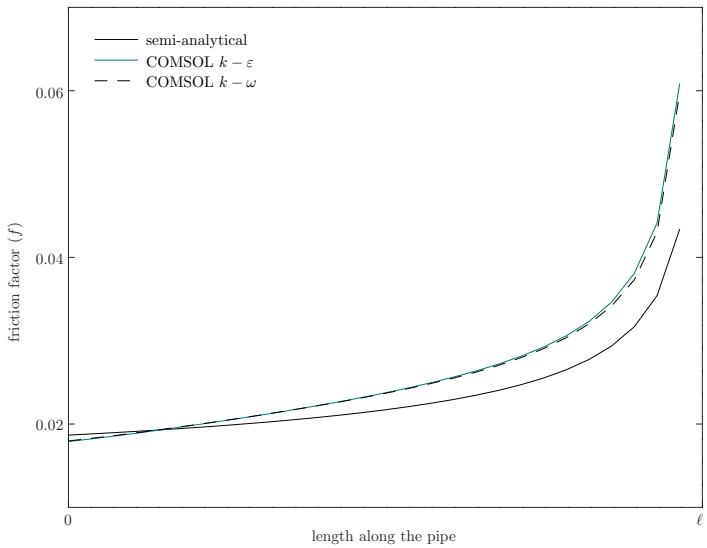

Figure 3.6: Longitudinal variation of friction factor for two different turbulence models in COMSOL compared with the semi-analytical solution at $p_o = 100.8$kPa. The values $x = 0$m and $x = l = 420$m corresponds to the outlet and the blocked end of the pipe respectively.

In both models, the friction factor is computed using Eq. (2.13) using the Reynolds number variation. Figure (3.6) shows the friction factor profile along the centerline of the well using two models. The two turbulence models agree exceptionally well and there is a good quantitative agreement between the semi-analytical and COMSOL solutions. This confirms that the frictional losses are addressed in the semi-analytical model and the impact on the COMSOL pressure profiles as shown in Figure 3.3(b) is not related to the friction factor. These effects were not addressed in the semi-analytical model and are at the core of its limitations. For a realistic description of the flow field within the well, Figure (3.6) is reminiscent of the necessity to include ingress turbulence effects.

3.2.2 Radial Variation

Pressure

Figure 3.7(a) shows the continuity of pressure along a straight ray from within the pipe through the slit to the immediately adjacent gravel layer for three slit sections along the

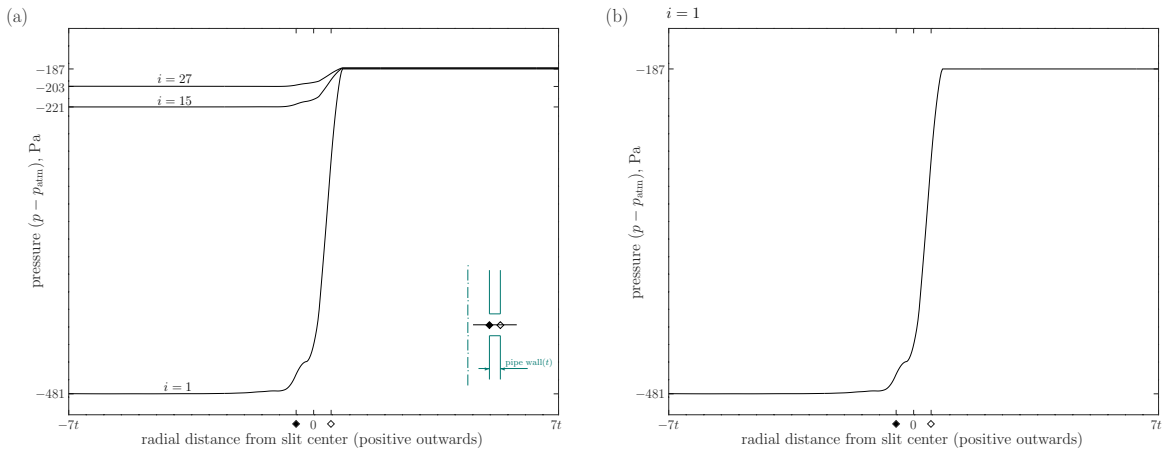

Figure 3.7: Radial pressure profiles across three slit sections: $i = 1$, 15 and 27, counting from the outlet at $p_o = 100.8$kPa (a) and the radial pressure profile across the slit section, $i = 1$ from the outlet at $p_o = 100.8$kPa (b). The thickness of the pipe is t. Values of r with $r < \blacklozenge < 0$ and $r > \diamond > 0$ represent the pipe and gravel medium respectively.

length of the well. The biggest gradient of pressure corresponds to the slit section that is closest to the outlet. At this section, the change in pressure is approximately equal to the pressure change along the length of the well at a given outlet suction (Figure 3.3). At the remaining slit sections ($i > 1$) further from the outlet, the local suction strength decays. Also the change of pressure is higher near the first slit section, and the majority of this change happens locally over a very small length scale, i.e pipe wall thickness, the radial dimension of the slit. At either side of the pipe wall, i.e within the porous medium on the right and pipe on the left, the pressure can be seen to remain virtually constant, but sub-atmospheric. The radial dimensions of porous media and the pipe are much larger than those of the slit. As a result, the fluid accelerates rapidly in the proximity of the ingress apertures as is seen from the sharp pressure gradients as the fluid enters the pipe. Similar to a jet injection, the sharp change in pressure is due to the effects of turbulence and mixing, where the two streams of different local velocities mix together within the well.

Figure 3.7(b) shows similar profile at the closet slit to the outlet at a much weaker suction of 100.8kPa. The sub-atmospheric pressure within the porous media is shown to depend on the suction within the well. The abrupt adjustment of pressure seen in both figures is called the boundary layer type behaviour.

Velocity

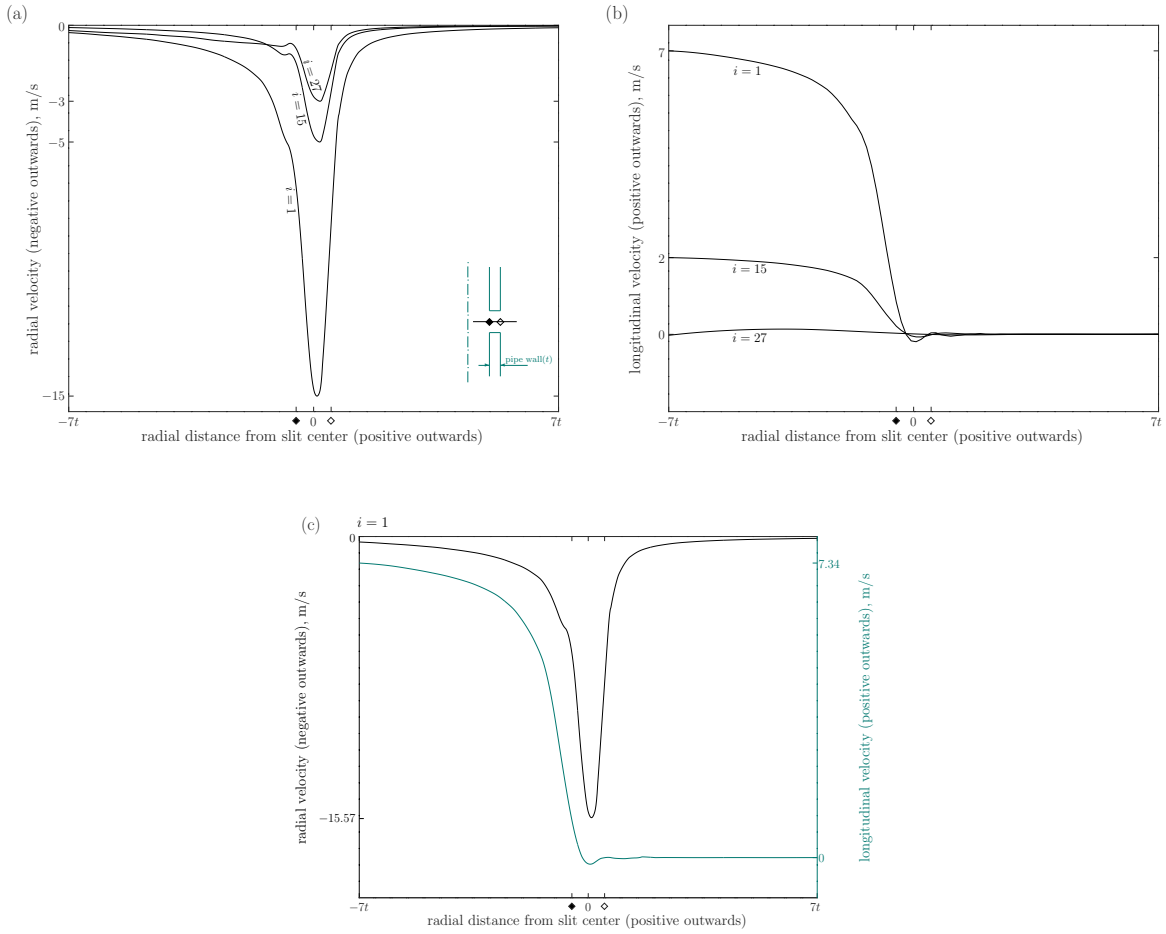

Figure 3.8: Radial velocity components (a), longitudinal velocity components (b) across the three slit sections: $i = 1$, 15 and 27, counting from the outlet at $p_o = 100.8$kPa and velocity components across section $i = 1$ from the outlet at $p_o = 100.8kPa$ (c). The thickness of the pipe is t. Values of r with $r < \blacklozenge < 0$ and $r > \diamond > 0$ represent the pipe and gravel medium respectively.

Figure 3.8 shows the components of the velocity at different slit sections along the length of the well at different outlet vacuum values. The radial component of velocity in Figure 3.8(a) shows that the gas accelerates towards the narrowest geometry indicated by the abrupt change in its magnitude over the very small width of the pipe wall. At either side of the pipe wall, this component decays to zero. The magnitude of the radial component can also be seen to decrease at further slit sections from the outlet. This behaviour is qualitatively similar for all the radial components at each slit sections and

is not shown here.

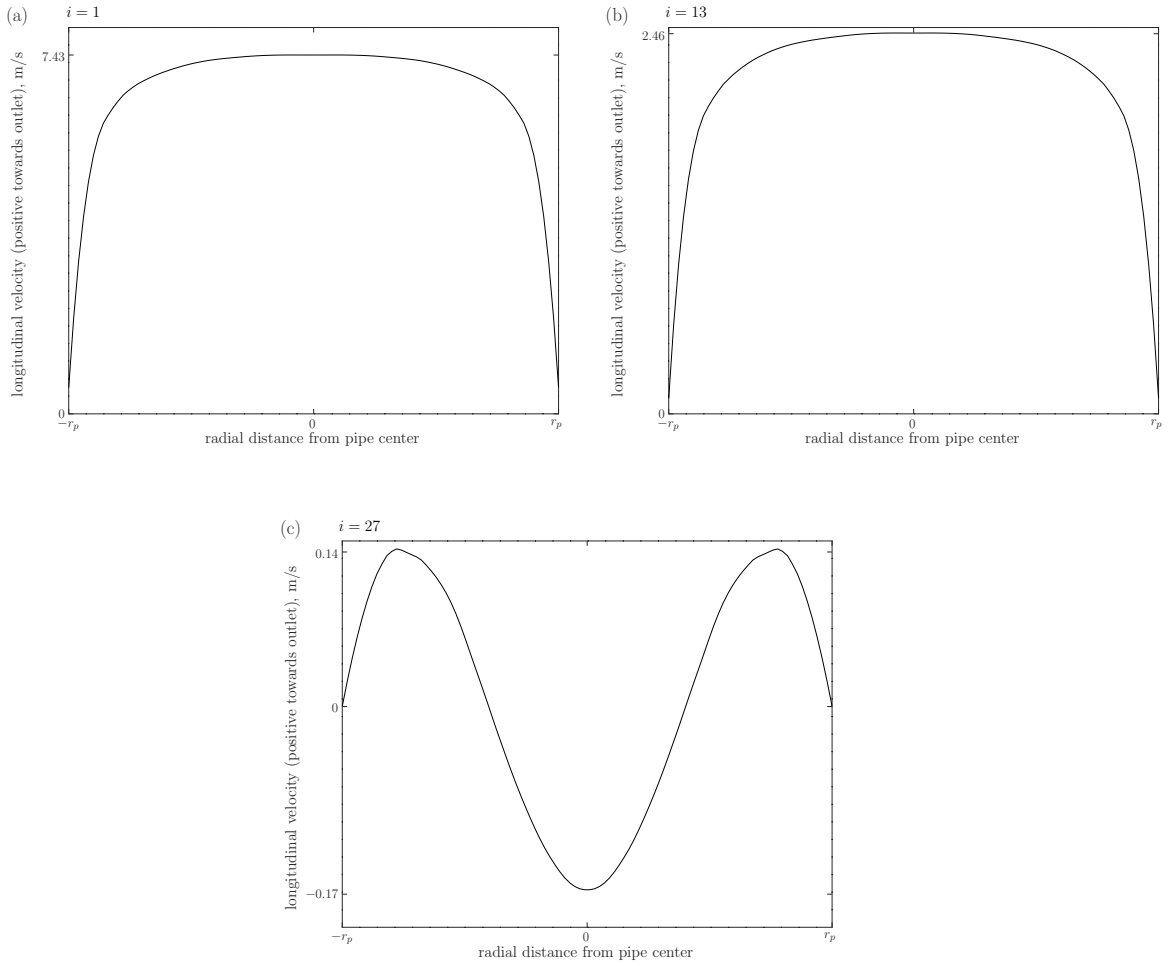

Figure 3.9: Velocity profiles within the pipe at the slits: $i = 1$ (a), 13 (b) and 27 (c) from the outlet at $p_o = 100.8$kPa. The radius of the pipe is r_p.

The sharp pressure gradient within the narrowest dimension shown in Figure 3.7, is responsible for the abrupt acceleration of the gas into the slit. Within the pipe, the radial component diminishes and the longitudinal component dominates the flow. This effect can be seen in the developing longitudinal component of velocity as shown in Figure 3.8 and 3.9. At $i = 27$, the gas flows towards the blocked end as seen in the Figure 3.9(c). This region acts as a *recess zone*. To verify whether steady state conditions were satisfied, the net mass flow rate within this zone was computed from the integration of the velocity field within the COMSOL. This was done at different sections within the zone. This zone is comprised of a pipe segment where one end is blocked and the other end is open. At

the open end, a section extended radially from the center of the pipe to the inner edge of the pipe. Next section was $10t$ distance away from the slit at $i = 27$ towards the recess zone. The five sections followed parallel to the two section at 407.5m, 410m, 412.5m, 415m and 417.5m in the well. The mass flow rates at the aforementioned sections are listed in Table 3.1. Except for the first two sections, the mass flow rates is numerical zero. The values at first two sections might be attributed to the thinner boundary layer formation or to the limitation of the solver used in COMSOL. Nontheless, the remaining mass flow rates within this zone substantiates that no mass was accumulating within this zone. As more mass of the gas enters the well however, the momentum of the flowing gas increases as indicated by the developing velocity profiles within the pipe domain as shown in Figures 3.9. At $i = 1$, the closest slit section from the outlet, the longitudinal component develops into a fully turbulent pipe flow profile as given.

No.	Sections at (m)	Mass flow rate (kg/s)	Note
1.	405.001	9.4×10^{-4}	$405 + (w/2)$
2.	405.016	-1.2×10^{-5}	$405 + 10t$
3.	407.5	-2.9×10^{-10}	numerical zero
4.	410	-7.6×10^{-12}	numerical zero
5.	412.5	1×10^{-10}	numerical zero
6.	415	-2.8×10^{-11}	numerical zero
7.	417.5	-3.6×10^{-11}	numerical zero

Table 3.1: Mass flow rate at different sections in the *recess zone*. The width of the slit w is calculated from Eq. 2.2 and the thickness of the pipe wall t is given in Table 2.1.

3.2.3 Optimization Considerations

The results given in the earlier sections show that the *head loss* due to ingress apertures is on par with the frictional losses within the pipe. To analyze the impact of ingress more carefully, the design parameters such as aperture size and frequency of perforations were varied. Two separate modifications were studied: the slit width was doubled, i.e $n_h \mapsto 2n_h$ and the frequency of the perforations was increased such that $N \mapsto 2N + 1$. Both configurations have identical total intake area, and it is possible to compare aperture traversing profiles at matching longitudinal positions as slit locations coincide at every other index i. Figure 3.10(a) shows the pressure profiles within the well for all configurations for the fully turbulent and quasi-1D models. In the COMSOL model the

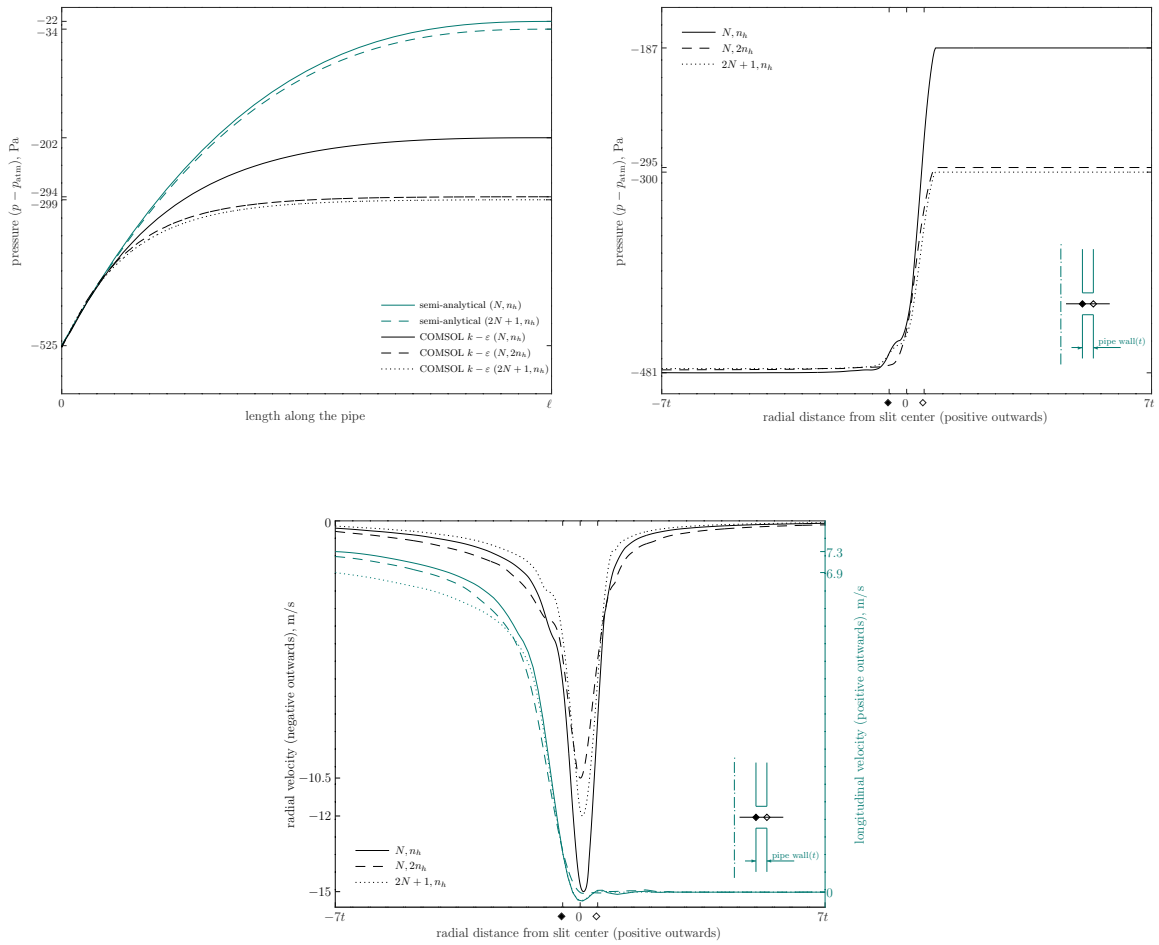

Figure 3.10: Longitudinal pressure variation along the well center line (a), pressure (b) and velocity components (c) along the center line of first coincident set of slits.

overall head loss in the well decreases due to increased intake area in both cases. The predicted decrease is very similar for both geometric modifications, allowing an inference that the intake ratio is the main parameters affecting the overall head loss in the well. Thus both geometric modifications can be expected to be equivalent for all practical purposes. However the same effect was only reflected in a minor deviation due to fluid compressibility in the semi-analytical model. Figure 3.10(b) shows the pressure profiles at the first coincident set of slits. It can be seen that the pressure jump is diminished with the increase in the total intake area, and both modified configurations yield a virtually identical head loss. The pressure profiles show that it might be beneficial to increase the intake area, but comparison of radial velocity components in Figure 3.10(c) show that

when the size of a sit is doubled, i.e. $n_h \mapsto 2n_h$, there is a reduction of the maximal velocity. However, this reduction was much higher than when the frequency of the slits was increased ($N \mapsto 2N + 1$). Even though one might expect that the maximal velocity would be roughly halved when number of perforations were increased, the results show that the reduction in velocity is even lower than when the slit sizes were doubled. From the figure, it can be seen that the flow inside the well is much faster for $n_h \mapsto 2n_h$ configuration, whilst its maximal radial velocity is smaller. In light of above, there should be an optimal configuration, where energy dissipation due to mixing at the perforated sections is minimal.

3.2.4 Meshing and Mass conservation

Mesh	Minimum element size	in w	in t
Unrefined	0.02m	$12.6w$	$2.8t$
Refined	2×10^{-6}m	$0.0013w$	$0.0003t$

Table 3.2: Element size parameters of the mesh used in COMSOL.

As the COMSOL model uses the finite element method to solve the governing fluid flow equations, the mesh resolution strongly impacts the precision of the variables computed. Away from the boundaries, triangular elements were used. These elements were refined to achieve appropriate precision in the solution at the contiguity boundaries between the flow domains. The relevant element size parameters for two meshes used in COMSOL are listed in the Table 3.2. Figure 3.11 shows the two mesh resolutions near the slits, which was obtained by using the combination of COMSOL's inbuilt meshing function with custom changes to increase the resolution at the narrowest region. Figure 3.12 shows that the pressure variable computed within the pipe on the left and within the porous medium on the right approaches the true limiting solution as the grid was refined. This behaviour was also observed for the velocity profiles and is not shown here.

To validate the integrity of the COMSOL model and to see whether the coupling between the porous media and turbulence models was adequately done, mass conservation was verified for the whole system. The conservation principle implies that the mass of gas generated from the landfill waste must be equal to the mass of gas drawn out from the outlet. Mass flow rates were computed from the line integration of the velocity profile at the outlet within COMSOL and by using the custom Octave function given in Appendix

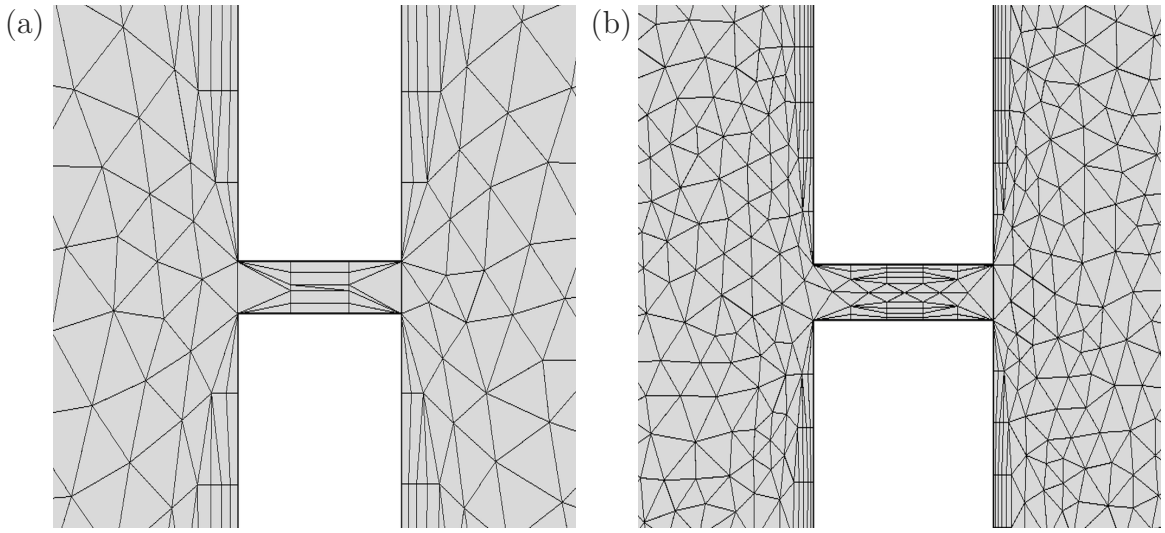

Figure 3.11: Unrefined (a) and refined mesh (b) resolutions used in the COMSOL. cf. Table 3.2

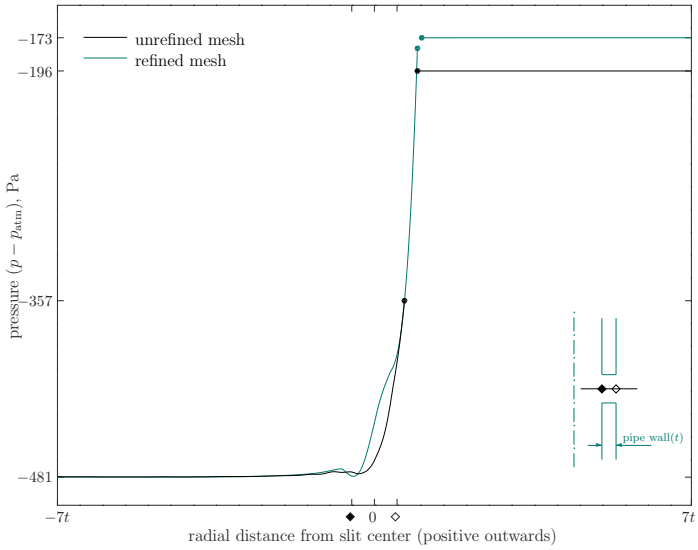

Figure 3.12: Radial pressure profiles across the slit section: $i = 1$, counting from the outlet using two mesh resolutions at $p_o = 100.8$kPa. The thickness of the pipe is t. Values of r with $r < \blacklozenge < 0$ and $r > \diamond > 0$ represent the pipe and gravel medium respectively.

A.4 that is based on Eq. (2.20). The values of mass flux at the outlet obtained from Eq. (2.20) and COMSOL were 0.143766kg/s and 0.145142kg/s respectively. These values of mass fluxes matched to the mass generated in the waste domain by (2.21) at 0.145142kg/s up to two and six significant figures respectively. The former value was computed by

simple trapezoidal integration of a discrete velocity profile output from COMSOL and did not include appropriate interpolation within the mesh elements. This indicates that the coupling of the two different flow domains –porous media and pipe– was accurate and that the model predictions are limited only by its assumptions.

3.2.5 Pipe Juncture Model

To address the effects of ingress holes in the semi-analytical model of the horizontal well, the equations given in 1.1.4 were used. An additional head loss parameter was introduced such that a pressure loss due to mixing could be incorporated at each perforated section. Similar to the jet system, the pipe juncture equations attempt to capture the losses due to mixing of the fluid streams and the 90° directional change, both obvious characteristics of horizontal well flow system.

The resistance coefficients that appear in Eqs. (1.2a) – (1.2e), were incorporated in the semi-analytical model. The coefficients for the branch $\zeta_{c.b}$, and main passage $\zeta_{c.s}$, were obtained using the empirical relations given for the discharge and cross-sectional area ratios at the junction. These ratios for the horizontal well were computed via the relevant area ratios and the mass flow rate at the ingress. However the values of coefficients such as A and 1.55 in Eq. (1.2b), were fitted specifically for the pipe junctions. Conceptually it is possible to suggest new values for these empirical coefficients to suit the current system.

An attempt was then made to reconcile the semi-analytical and COMSOL models by fitting the foregoing coefficients so that the semi-analytical solutions would agree with/match the COMSOL solution. The set of coefficients can be successfully fit to one fixed well configuration, i.e. given values of parameters such as outlet pressure, media permeabilities and mass generation rate. This confirms the qualitative similarity between the pipe juncture / jet flow fields and the local description of entry into a horizontal well. However, when the basic configuration parameters were varied, the fitted set of coefficients were found to be globally inapplicable. This sensitivity means that the horizontal well is a more complicated system, where one set of empirical coefficients cannot capture the losses faithfully over a realistic, practicable parameter space. Thus a computationally intensive approach was found to be essential in capturing the fluid behaviour near the narrow apertures of the horizontal well.

4. Summary

Landfill gas is deemed essential for collection because of its threat to the environment and global climate. The desire to collect this gas has also grown significantly because of its potential as a renewable energy resource. The collection is done through well systems. Horizontal wells, consisting of perforated pipe embedded horizontally within the landfill mass, are a common engineering solution, despite a lack of proper mathematical flow description. An efficient collection system can be designed by optimising the well's operational parameters. Introduction of possible improvements hinges on understanding the behaviour of the gas as it traverses the complex man-made flow domains. One needs to understand the interaction of the gas and its surrounding boundaries to provide an accurate descriptions of the flow. Within the porous media the permeability of the matrix is the governing flow parameter. Within the well the interaction of the fluid layers during mixing between themselves and also with the pipe boundary underpins the generated flow field.

Landfill gas enters the horizontal well through small perforations provided along its length. The gas is drawn through these holes by applying suction at the outlet of the well. The other end is blocked and is responsible for maintaining sub-atmospheric pressure within the well and its surrounding porous media. At the holes, the fluid pattern is quite complicated as described by the studies on similar systems such as jets, whose main difference is that a jet is injected into the cross flow (Forney *et al.*, 1999). Numerous studies have described the nature of underlying structures generated as a result of mixing between the two fluid streams, without any agreement on one common model for such fluid interactions. These studies attempt to provide structure to an apparently chaotic flow, i.e. turbulent flow (Roshko, 1976). The flow of the landfill gas at the apertures of a horizontal well undergoes a contraction followed by subsequent expansion within the well (Idelcik, 1966). The fluid stream mixes with the cross flow, changes its direction and flows towards the outlet. All these processes near the holes occur via viscous shearing between the fluid layers, inducing 3D vortical structures, a characteristic specific to turbulent flows (Dimotakis, 2000). These structures manifest a multitude of characteristic length scales (Broadwell & Breidenthal, 1984). To address these effects, one must perform a detailed analysis on the underlying flow structures. In order to explore the turbulence effects at

the ingress into the horizontal well, RANS equations were solved with two turbulence closure models using the finite element solver COMSOL. The results were then compared with the semi-analytical model that excluded the ingress effects.

The semi-analytical model was based on a quasi-1D geometry formulation of the horizontal well (Nec & Huculak, 2019). It comprised of axisymmetric slits of an area equivalent to that of a given number of circular holes in a cross section. The frictional losses were computed for each pipe segments and the landfill was discretized into sequence of discs aligned with each slits, where pressure continuity was enforced. This geometry is simplistic compared to the 2D axisymmetric model constructed in COMSOL, where the solid pipe boundary was accounted for in both coupled types of flow and continuity of pressure was maintained only at the apertures. Because of the geometrical limitations of the semi-analytical model, the ingress turbulence effects could not be incorporated. The fully turbulent results were obtained for a range of outlet pressure values, mass generation rates and permeabilities of the porous matrices. The comparison plots for the semi-analytical and COMSOL solutions show the impact of conceptual limitations of the semi-analytical model as discussed.

The ingress effects impact the overall well pressure distribution. The semi-analytical model overestimates the head loss in the well and also the pressure levels within the porous domains, and overlooks the strong variation near the apertures. The impact on well pressure due to ingress turbulence effects is further substantiated by the similar friction factor profiles obtained using two solutions. This formulation also impacts the Reynolds number: the semi-analytical prediction is an almost linear dependence, whereas the fully turbulent solutions give fully non-linear profiles. Abrupt velocity and pressure changes occur near the slits, across a small length scale, i.e pipe's wall thickness. The fluid accelerates rapidly with the radial component of the velocity increasing abruptly at the narrow passage and decaying to zero at the well centerline thereupon. The gas entering the farthest slit is seen to turn away from the outlet into the well's "recess zone", although this effect slowly diminishes downstream as more fluid mass entering the well contributes to a full development of the flow.

The two turbulence models tested yielded very similar results. Solution consistence was demonstrated via mesh refinement, verifying continuity of the flow field (pressure and velocity) between two systems of flow domains. Overall mass conservation was confirmed: the gas generated within the given volume of the landfill was equal to the outflow at the outlet. An attempt to address the limitations of the semi-analytical formulation by

incorporating an ad-hoc model qualitatively following the empirical pipe juncture setting was unsuccessful owing to its unduly sensitivity, attesting to the complexity of the flow field in this system.

This study shows the importance of careful ingress flow modeling to account for the turbulence effects due to apertures in a landfill gas collection system. These effects are shown to impact the global design of the horizontal wells. The flow field around the ingress of a horizontal well is more complex than jet systems, notorious for computationally intensive numerical techniques used in an attempt to provide an accurate description of turbulence and its underlying flow structures. To attain qualitative insight into turbulence due to holes in the horizontal well system, basic $k - \varepsilon$ and $k - \omega$ turbulence models (Wilcox *et al.*, 1998) were found sufficient. Numerical solutions of the governing equations (Navier-Stokes and Darcy's law) reveal influential changes over very small spatial scales near the ingress. The cumulative changes affect directly the outlet suction applied to extract the gas, which is the single most important parameter available to the landfill well operators. When this controllability via the outlet vacuum diminishes, one of the alternative control mechanism can be to increase the perforation frequency. The results imply that this strategy might improve the overall head loss in the well up to a certain point, and adding more apertures will incur higher losses since the incoming stream of fluid must mix and adjust its flow direction. The semi-analytical model for this well system is shown to be limited by its geometrical formulation in addressing ingress turbulence effects, resulting in overestimation of the pressure field in and around the well. Whilst this might serve as a simple tool for an initial design, the qualitative findings from COMSOL revealed that the influence of ingress turbulence is significant and should not be neglected for a realistic representation of flow in the horizontal well.

Appendices

A. Octave Programs

A.1 Smoothing function

```
function [yi, xi] = smooth(x, y, xi, w, d)

x = x(:); y = y(:); xi = xi(:);

%%Presumption length(x) = length(y)
ly = length(y);

%%presumption w integer, preferably odd
wr = round(w / 2); wf = floor(w / 2);
yi  = xi * 0;

for i= wr : ly - wf
  p(i, :) = polyfit(x(i - wr + 1 : i + wf), y(i - wr + 1 : i + wf), d);
  if (i == wr)
  yi(1 : i)=polyval(p(i, :), xi(1 : i));
  elseif (i == ly - wf)
  yi(i : end) = polyval(p(i, :), xi(i : end));
  else
  yi(i) = polyval(p(i, :), xi(i));
  end
end
endfunction
```

A.2 Colebrook function

```
function y = colebrook_f(prm, f)
    %%Roughness parameter and Reynolds number
    epsilon = prm(1); Re = prm(2);

    %%Colebrook equation
    y = 1 ./ sqrt(f) + 2 * log10(epsilon / 3.7 + 2.51 ./ (Re * sqrt(f)));
endfunction
```

A.3 Calculation of Reynolds number and friction factor

```
%%Longitudinal velocity profile data
file = load ("Vel_long_100600_tur_k-e.txt");
x1 = file(:,1);
y1 = file(:,2);
file = load ("Vel_long_100600_tur_k-w.txt");
x2 = file(:,1);
y2 = file(:,2);

%%Longitudinal pressure profile data
file = load ("Pre_long_100600_tur_k-e.txt");
x3 = file(:,1);
y3 = file(:,2);
file = load ("Pre_long_100600_tur_k-w.txt");
x4 = file(:,1);
y4 = file(:,2);

%%Longitudinal pressure profile data at 5m. radial distance
file = load ("Pre_long_100600_tur_k-e_5r.txt");
x5 = file(:,1);
y5 = file(:,2);
```

```
wi = 2000; %Window size
dg = 2; %Degree of freedom

%%Smoothing
[yi1,xi1] = smooth(x1,y1,x1,wi,dg);
[yi2,xi2] = smooth(x2,y2,x2,wi,dg);
[yi3,xi3] = smooth(x3,y3,x3,wi,dg);
[yi4,xi4] = smooth(x4,y4,x4,wi,dg);
[yi5,xi5] = smooth(x5,y5,x5,wi,dg);

xii = zeros(n,1);
yii = zeros(n,1);

%%Sorting the data
for i = 0 : n
    k = i * l;
    [val1,idx1] = min(abs(k - xi1));
    [val2,idx2] = min(abs(k - xi2));
    [val3,idx3] = min(abs(k - xi3));
    [val4,idx4] = min(abs(k - xi4));
    xii1(i + 1, 1) = xi1(idx1);
    yii1(i + 1, 1) = yi1(idx1);
    xii2(i + 1, 1) = xi2(idx2);
    yii2(i + 1, 1) = yi2(idx2);
    xii3(i + 1, 1) = xi3(idx3);
    yii3(i + 1, 1) = yi3(idx3);
    xii4(i + 1, 1) = xi4(idx4);
    yii4(i + 1, 1) = yi4(idx4);
end

%%Density of the gas using pressure profile
rho_c = [yii3/(R*T) yii4/(R*T)];

%%Reynolds number using velocity profile and density
```

```
Re_c = [(rho_c(:,1).*abs(yii1)*d)/mu (rho_c(:,2).*abs(yii2)*d)/mu];

[nR,nC] = size(Re_c);

%%Calculation of friction factor from reynolds number.
for j = 1:nC
    for i = 1:nR;
        if Re_c(i,j) <= 1000
            f_com(i,j) = 64/Re_c(i,j);
        else
            f0 = linspace(10^(-4),0.1,1000);
            res = colebrook_f([epsilon Re_c(i,j)],f0);
            s = sign(res(1:end-1).*sign(res(2:end)));
            root_ix = find(s<0);
            if isempty(root_ix)
                error('Failure to find the solution');
                %y=100;
                return
            end
            f0 = [f0(root_ix) f0(root_ix+1)];
            f_com(i,j) = fzero(@(f_com) colebrook_f([epsilon Re_c(i,j)],f_com),f0);
        end
    end
end
```

A.4 Calculation of mass flux at the outlet

```
function y = OutletVelocity(vari, p_out, R, T)

    %% Radial distance at the outlet
    ra = vari(:, 1);

    %% Velocity magnitude at the outlet
    ve = vari(:, 2);

    ra = ra(1 : end) - ra(1); ve = ve(1 : end);
    ma = trapz(ra, ra .* ve) * 2 * pi;
    rhov = p_out / (R * T);

    %% Mass flux at the outlet
    y = ma * rhov;
endfunction
```

Bibliography

Bellos, V, Nalbantis, I & Tsakiris, G 2018 Friction modeling of flood flow simulations. *Journal of Hydraulic Engineering* **144** (12), 04018073.

Bevilaqua, PM & Lykoudis, PS 1971 Mechanism of entrainment in turbulent wakes. *AIAA Journal* **9** (8), 1657–1659.

Broadwell, JE 1982 A model of turbulent diffusion flames and nitric oxide generation. part i. *TRW Document* (38515-6001).

Broadwell, JE & Breidenthal, RE 1982 A simple model of mixing and chemical reaction in a turbulent shear layer. *Journal of Fluid Mechanics* **125**, 397–410.

Broadwell, JE & Breidenthal, RE 1984 Structure and mixing of a transverse jet in incompressible flow. *Journal of Fluid Mechanics* **148**, 405–412.

Chilton, TH & Genereaux, RP 1930 The mixing of gases for reaction. *AIChE Transaction* **25**, 102–122.

Churchill, SW 1973 Empirical expressions for the shear stress in turbulent flow in commercial pipe. *AIChE Journal* **19** (2), 375–376.

Churchill, SW 1977 Friction factor equation spans all fluid flow regimes. *AIChE Journal* pp. 91–92.

Colebrook, CF 1939 Turbulent flow in pipes with particular reference to the transition region between the smooth and rough pipe laws. *Journal of the Institution of Civil Engineers* **11**, 133–156.

COMSOL Inc. 2018 CFD module user's guide.

Dahm, WJA & Dimotakis, PE 1987 Measurements of entrainment and mixing in turbulent jets. *AIAA journal* **25** (9), 1216–1223.

Deardorff, JW 1970 A numerical study of three-dimensional turbulent channel flow at large reynolds numbers. *Journal of Fluid Mechanics* **41** (2), 453–480.

Dimotakis, PE 2000 The mixing transition in turbulent flows. *Journal of Fluid Mechanics* **409**, 69–98.

Durando, NA 1971 Vortices induced in a jet by a subsonic cross flow. *AIAA Journal* **9** (2), 325–327.

Eaton, JW, Bateman, D, Hauberg, S & Wehbring, R 2020 Gnu octave version 6.1.0 manual: a high-level interactive language for numerical computations. .

Emmons, HW 1951 The laminar-turbulent transition in a boundary layer-part i. *Journal of the Aeronautical Sciences* **18** (7), 490–498.

EPA-US 2012 Landfill gas energy utilization technologies. *International Best Practices Guide for LFGE Projects* pp. 33–50.

Fitzgerald, SD & Holley, ER 1979 Jet injections for optimum mixing in pipe flow. *NASA STI/Recon Technical Report N* **80**.

Forney, LJ, Feng, Z & Wang, X 1999 Jet trajectories of transverse mixers at arbitrary angle in turbulent tube flow. *Chemical Engineering Research and Design* **77** (8), 754–758.

Grant, HL 1958 The large eddies of turbulent motion. *Journal of Fluid Mechanics* **4** (2), 149–190.

Haaland, SE 1983 Simple and explicit formulas for the friction factor in turbulent pipe flow. *Journal of Fluids Engineering* **105** (1), 89–90.

Idelcik, IE 1966 Handbook of hydraulic resistance: coefficients of local resistance and of friction. *Tech. Rep.*. ERDA Div. Phys. Res.

Kamotani, Y & Greber, I 1972 Experiments on a turbulent jet in a cross flow. *AIAA journal* **10** (11), 1425–1429.

Konrad, JH 1977 An experimental investigation of mixing in two-dimensional turbulent shear flows with applications to diffusion-limited chemical reactions. PhD thesis, California Institute of Technology.

Konrad, JH & Brown, GL n.d. The effect of reynolds number and the mechanism for development of three dimensionality and fine scales in a turbulent shear flow. Unpublished.

Levin, SR 1935 Analiticheskoe opredelenie velichiny poter' napora v trolnikakh vytyazhnykh ventilyatsionnykh setei (analytic determination of the magnitude of head losses in y-branches of ventilating exhaust systems). *Otoplenie i ventilyatsiya (Heating and ventilation)* (7).

Levin, SR 1940 Soprotivienie troinikov vytyazhnykh vozdukhovodov (resistance of y-branches of exhaust air conduits). *Otoplenie i ventilyatsiya (Heating and ventilation)* (10–11).

Nec, Y & Huculak, G 2019 Landfill gas flow: collection by horizontal wells. *Transport in Porous Media* **130** (3), 769–797.

Orszag, SA 1970 Analytical theories of turbulence. *Journal of Fluid Mechanics* **41** (2), 363–386.

Patrick, MA 1967 Experimental investigation of the mixing and penetration of a round turbulent jet injected perpendicularly into a transverse stream. *Trans. Inst. Chem. Eng* **45**, 16–31.

Rathgeber, DE & Becker, HA 1983 Mixing between a round jet and a transverse turbulent pipe flow. *The Canadian Journal of Chemical Engineering* **61** (2), 148–157.

Roshko, A 1976 Structure of turbulent shear flows: a new look. *AIAA journal* **14** (10), 1349–1357.

Serghides, TK 1984 Estimate friction factor accurately. *Chemical engineering (New York, NY)* **91** (5), 63–64.

Smagorinsky, J 1963 General circulation experiments with the primitive equations: I. the basic experiment. *Monthly weather review* **91** (3), 99–164.

Stanley, SA, Sarkar, S & Mellado, JP 2002 A study of the flow-field evolution and mixing in a planar turbulent jet using direct numerical simulation. *Journal of Fluid Mechanics* **450**, 377–407.

Swanee, PK & Jain, AK 1976 Explicit equations for pipeflow problems. *Journal of the hydraulics division* **102** (5).

Taliev, VN 1952 Raschet mestnykh soprotivlenii troinikov (calculation of the local resistances of y-branches). *Gosstroiizdat (State Committee for Publishing in the Soviet Union)* .

Taneda, S 1959 Downstream development of the wakes behind cylinders. *Journal of the physical society of Japan* **14** (6), 843–848.

Theodorsen, T 1952 Mechanism of turbulence. proc. 2nd midwestern conf.

Townsend, AA 1956 The structure of turbulent shear flow. *Journal of Fluid Mechanics* **1**, 554–560.

Wilcox, David C *et al.* 1998 *Turbulence modeling for CFD*, , vol. 2. DCW industries La Canada, CA.